Universidade de São Paulo
Instituto de Astronomia, Geofísica e Ciências Atmosféricas
Departamento de Astronomia

Ivan Almeida

Winds and feedback from supermassive black holes accreting at low rates

São Paulo

2019

Ivan Almeida

Winds and feedback from supermassive black holes accreting at low rates

Dissertation presented to the Astronomy department of the Institute of Astronomy, Geophysics and Atmospheric Sciences of the University of São Paulo as partial requisite to obtain the Master in Sciences title.

Concentration Area: Astronomy
Advisor: Prof. Dr. Rodrigo Nemmen

Corrected version. The original is available in IAG-USP.

São Paulo
2019

To Jade and Rosa...

Acknowledgements

This dissertation is a brief synthesis of two years of work, it is a presentation of the results. Scientific results carry the relevant information about the studied topic, however they do not talk about the history behind their production. In these two years I was helped by a lot of people – and I hope that I helped them too. In a future publication of the results, there will not be any mention of these important people, but fortunately I can do it here.

First of all I thank all the members of the IAG Black Hole group. Starting with my advisor Prof Rodrigo Nemmen, who during this time deposited trust in me and in my abilities and gave me important advice about research, career and how to be a proper scientist, I am very grateful to you. Thanks to all my group colleagues (and ex-colleagues): Artur, Fabio, Gustavo, Raniere, Roberta and Maria Lúcia that helped me a lot and gave to me amazing moments of learning and friendship.

Muito obrigado to my family that always supported my crazy decision to become an astrophysicist. I can not thank them in English because they deserve to understand my words. They always encouraged me to search knowledge and feed all my curiosity despite our financial status. I am totally grateful to my parents Claudemir and Joana that sacrificed a lot of things to give me the opportunity to reach this point.

Thanks to Luis Kadowaki that helped me a lot with the simulation setups and with all the numerical problems that haunted me during this work. A special thanks to the guys responsible for the maintenance of the computers in IAG and the maintenance of Alphacrucis and AGUIA clusters, this work would have been impossible without these heroes.

Thanks to all my IAG friends for making the postgraduate life better, you made the

corridors of IAG a very friendly place. I need to thank all my external friends, the ones that I play football with, the Tucuruvi team, my old friends from IFSP-SP and IFUSP (our pub table is always full of great people). You all always renew my humour and make me forget and surpass the bad moments in the last two years.

last, but not less important, I am grateful to my cats. In all the moments that I was sad or uncomfortable I hugged them tight –despite their complaints– and everything became better.

This work was supported by FAPESP (Fundação de Amparo à Pesquisa do Estado de São Paulo) under grants 2016/24857-6 and 2017/01461-2. This work has made use of the computing facilities of the Laboratory of Astroinformatics (IAG/USP, NAT/Unicsul), whose purchase was made possible by the Brazilian agency FAPESP (grant 2009/54006-4) and the INCT-A. Research developed with the help of HPC resources provided by the Information Technology Superintendence of the University of São Paulo.

“*It was never about the money, it was always about the fun.*”

Kouta Hirano

“*Astronomers, like burglars and jazz musicians, operate best at night.*”

Miles Kington

Abstract

The local universe is dominated by quiescent galaxies with little or no ongoing star formation. Once star formation has been shut down in a possible quasar phase, energy feedback in the form of outflows from a supermassive black hole (SMBH) accreting at a low rate is one of the leading candidates for heating up or removing gas accreted afterwards. In this work we performed hydrodynamic simulations of radiatively inefficient accretion flows around supermassive black holes and investigate the generation of outflows by the accretion flow. We found that hot accretion flows can produce powerful subrelativistic winds that carry considerable amounts of energy away and they can provide feedback inside the host galaxy.

Resumo

O universo local é dominado por galáxias quiescentes com pouca, ou nenhuma, taxa atual de formação estelar. Uma vez que a formação estelar é suprimida numa possível fase de quasar do núcleo ativo da galáxia, o *feedback* de energia na forma de *outflows* do buraco negro supermassivo acretando a pequenas taxas é um dos principais candidatos a aquecer ou remover o gás do sistema. Nesse trabalho, executamos simulações hidrodinâmicas de escoamentos acretivos radiativamente ineficientes ao redor de buracos negros supermassivos e investigamos a geração de *outflows* pelo escoamento. Encontramos que escoamentos acretivos quentes podem produzir ventos subrelativísticos poderosos que carregam para fora consideráveis quantidades de energia e que podem providenciar *feedback* dentro da galáxia hospedeira.

List of Figures

List of Tables

Contents

List of Abbreviations

- RIAF – Radiatively Inefficient Accretion Flow
- ADAF – Advection Dominated Accretion Flow
- ADIOS – Adiabatic Inflow-Outflow Solution
- BH – Black Hole
- SMBH – Supermassive Black Hole
- HD – Hydrodynamics
- MHD – Magnetohydrodynamics
- GR – General Relativity
- GRMHD – General Relativistic Magnetohydrodynamics
- AGN – Active Galactic Nuclei
- LLAGN – Low-Luminosity Active Galactic Nuclei

Chapter 1

Introduction

Black holes (BHs) are one of the most famous results from General Relativity (GR)– they are objects that cannot exist in a Newtonian universe. They are the solution of the Einstein field equations for a point mass particle, found originally by Karl Schwarzschild in the war front during the First World War. Since those chaotic times, scientists elaborated diverse models and made several discoveries about this topic. We discovered that these objects are not just an odd mathematical solution of the GR equations, but they *de facto* exist in nature (Schmidt, 1963; Thorne and Price, 1975). In the last decades, BHs become very important astrophysical objects, they are observed in our Galaxy and mainly as extragalactic sources, associated to very energetic astrophysical events like supernovae, gamma-ray bursts, active galactic nuclei, and others (Meier, 2012). Besides the traditional electromagnetic astronomy, the dawn of gravitational wave astronomy with the very recent LIGO results (Abbott et al., 2016) highlights the importance to study BHs, in order to understand gravity and the universe itself.

BHs appear in different sizes across the universe, their size is given by the famous Schwarzschild radius, which is the size of the event horizon of the BH which is directly linked to its mass:

$$R_S = \frac{2GM}{c^2}. \tag{1.1}$$

The Schwarzschild radius is essentially the radius of a object with mass M, and without rotation, in that the escape velocity from its gravitational field is equal to the speed of light (c); here G is the gravitational constant. Once inside R_S only superluminal particles could escape from the BH–which relativity forbids.

The Schwarszchild solution depends only of the mass of the BH, the mass defined all the properties of the space-time around the object, this solution is presented as the

Schwarzschild metric. Posterior works enhanced this scenario, and stated that the BH can be defined by three main parameters: Mass, spin (angular momentum) and charge (Newman et al., 1965). For astrophysical purposes, we do not consider the BH charge, we assume that the big structures of the universe are all neutral.

There are two big populations of BHs in the universe, they were divided by their mass, the stellar BHs have masses between 5 to several tens solar masses and supermassive BHs (SMBHs) with masses above a million of solar masses – intermediary mass BHs are never observed, but there is no reason to believe they do not exist. Observations support that in the nucleus of most galaxies–except some dwarf galaxies– there is, at least, one SMBH (Ferrarese and Ford, 2005). Here, in this work, our focus is on the SMBHs.

Once a BH becomes surrounded by gas, it starts to accrete the available material (Frank et al., 2002). Roughly speaking the BH starts to swallow the material around, this process occurs naturally both to stellar or supermassive BHs. The accreting stellar BHs can be seen in the so called high-massive x-ray binaries; for the case of SMBHs we have the phenomena called active galactic nuclei (AGN), which is the state when the SMBH are accreting available gas from the galactic nucleus –the origin of the gas could be from galactic mergers, stellar tidal disruptions, or material that come from the galaxy and fell into the central SMBH via dynamical friction. Accretion processes in AGNs are the main topic of our work.

AGNs are very complex systems. The unified model–a model that, as the name says, is an effort to explain them in an unified way–is display in figure 1.1. It is composed by an accreting black hole surrounded by a big dust torus, this system could present a relativistic jet too (Beckmann and Shrader, 2012; Netzer, 2015). The accretion disc is in the core of the AGN and corresponds to a very small region, the average size of the accretion disc is in subparsec scales, which is currently not possible to resolve with our telescopes –nowadays we are starting to see these regions of SgrA* with GRAVITY and the Event Horizon Telescope collaborations (Doeleman et al., 2008; Abuter et al., 2018), but it is still a big challenge do the same for extragalactic sources (cf. Sturm et al. 2018). The dust torus is a irregular structure in parsec scale that surrounds the accretion disc. The relativistic jet is a structure that arises from the accretion disc due to relativistic effects of the plasma that fell into the BH, jets are probably the most famous feature of an AGN and can reach Mpc scales.

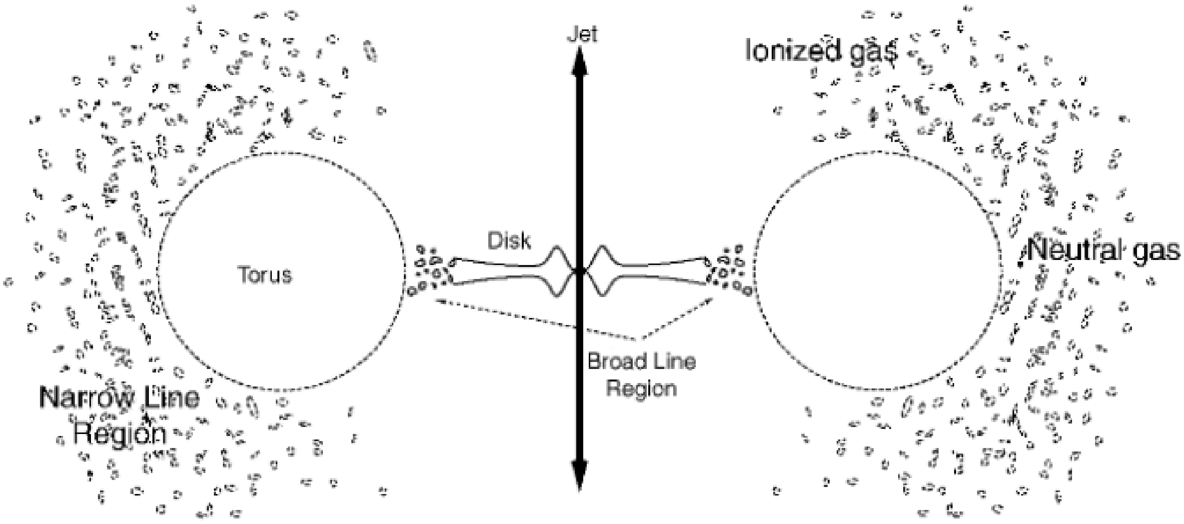

Figure 1.1: Simplified sketch of the AGN unified model extracted from Schneider (2006) (figure 5.25).

The types of AGNs are very diverse, with several different categories such as quasars, Seyfert galaxies, radio galaxies, blazars etc. Our study was focused in low-luminosity AGNs (LLAGNs), a very common type of AGN in the nearby universe. LLAGNs, as the name reveals, are ones with much smaller luminosity than quasars (and other AGN types). They normally are present in quiescent galaxies. The smaller luminosity is an indicative that the SMBH is underfed, compared to a SMBH in a quasar (cf. section 1.1).

Quiescent galaxies are the ones with very small star formation rates, and this is the most common type of galaxy at low redshift, dominating the local universe. These galaxies probably in the past experimented a phase with higher star formation rates that have been shut down times later. One open question is: What are the mechanisms responsible for shutting down the star formation? The answer probably is related to the central engine of AGNs, the accretion disc.

1.1 *Accretion physics*

Accretion is a very common feature in universe. When we analyze how baryonic matter interacts with itself, we will find that in presence of a massive central object surrounded by gas, a natural way that the gas falls into the central object is via accretion discs. Accretion discs arise when a fluid with angular momentum is falling under influence of a gravitational field originating from the central object, or from a set of central objects. These discs can be present around stars, neutron stars and BHs.

When matter falls into a BH in a disk-like structure due to the barrier posed by angular momentum conservation it forms an accretion flow. Magnetic stresses in the ionized plasma introduce friction which allows the gas to flow in toward the BH (Balbus, 2003), i.e. the friction allows the fluid to lose angular momentum and falls into the central object. At the same time, these stresses convert some of the gravitational potential energy of the accretion flow into heat and can release a substantial fraction of its rest mass energy, providing the primary power source behind AGNs, black hole binaries and gamma-ray bursts (Meier, 2012).

The dynamics of the resulting accretion flow depends critically on whether the viscously generated thermal energy is radiated away (Abramowicz and Fragile, 2013). This is parameterized in terms of the radiative efficiency $\eta = L/\dot{M}c^2$ where L is the luminosity produced by the accretion flow and $\dot{M}$ is the mass accretion rate onto the BH. In figure 1.2 we divided the accretion flows around a BH according to the efficiency ϵ, we parameterized the values of accretion rate in function of the Eddington accretion rate, defined as

$$\dot{M} = \epsilon \dot{M}_{Edd} = \epsilon \frac{4\pi G M m_p}{\epsilon c \sigma_T}, \tag{1.2}$$

where M is the central object mass, m_p is the proton mass and σ_T is the Thomson cross section (Frank et al., 2002). For $\epsilon > 1$ we have super-Eddington accretion rates which are very high accretion rates leading to an extremely bright and uncommon object; quasars, the most brilliant AGNs, have in general $\epsilon \sim 0.1$ and are characterized by a thin disc. In this work, we are particularly interested in the regime of BHs accreting at low $\dot{M}$. At rates $\dot{M} \lesssim 0.01\dot{M}_{\mathrm{Edd}}$, the gas cannot radiate its thermal energy away and becomes extremely hot ($T \sim 10^{12}$ K), geometrically thick ($H \sim R$, H is the vertical disk thickness) and optically thin, giving rise to a radiatively inefficient accretion flow (RIAF) with $\epsilon \ll 1$ (Yuan and Narayan, 2014).

In figure 1.3 we show a simplified cartoon of the innermost part of one LLAGN. In the center of the system, surrounding the SMBH, there is a hot accretion disc, in RIAF mode and dominated by advection, where the energy is trapped inside the disc and it is advected with the flow to the SMBH, this is the called advection dominated accretion flow (ADAF). The model considers the jet, which is very common in LLAGNs, and an external

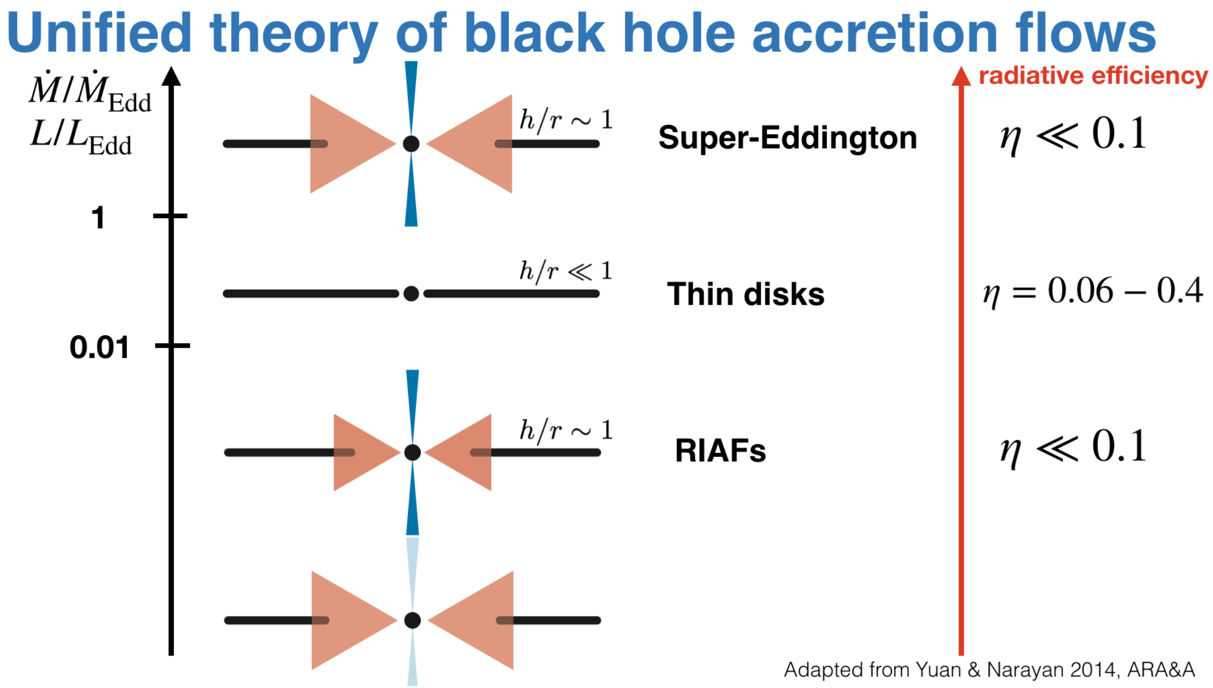

Adapted from Yuan & Narayan 2014, ARA&A

Figure 1.2: Scheme adapted from Yuan and Narayan (2014) showing the types of accretion discs in function of the efficiency parameter ϵ . The accretion rate determines the geometry of the accretion flow. Image courtesy of Rodrigo Nemmen.

thin disc, for some systems the observational contribution of the thin disc can be neglected, depending on the ADAF size (Nemmen et al., 2014; Almeida et al., 2018). It is expected from these system material ejection, from the jet and in the form of winds from the ADAF (Ichimaru, 1977; Narayan and Yi, 1994).

1.2 *RIAFs in the universe*

The first reason why the RIAF regime is important is simply because the sheer majority of SMBHs in the local universe–inactive galaxies and low-luminosity AGNs (LLAGNs)–are fed at low, sub-Eddington rates in comparison with massive BHs at high redshifts (Ho, 2008; Nemmen et al., 2014); therefore, understanding well the physics of RIAFs will allow a better comprehension of most SMBHs at $z \approx 0$, which are in the RIAF mode. The nearest example is Sagittarius A* (SgrA A*), the $4 \times 10^6\,M_\odot$ BH at 8kpc, in the center of Our Galaxy (Narayan et al., 1995; Yuan et al., 2003). Figure 1.4 displays the x-ray emission from the region.

SgrA* is an underfed SMBH with extremely low accretion rate of $\sim 10^{-6}\dot{M}_{Edd}$, which is a very low value even for a traditional LLAGN, but there is evidences that its activity

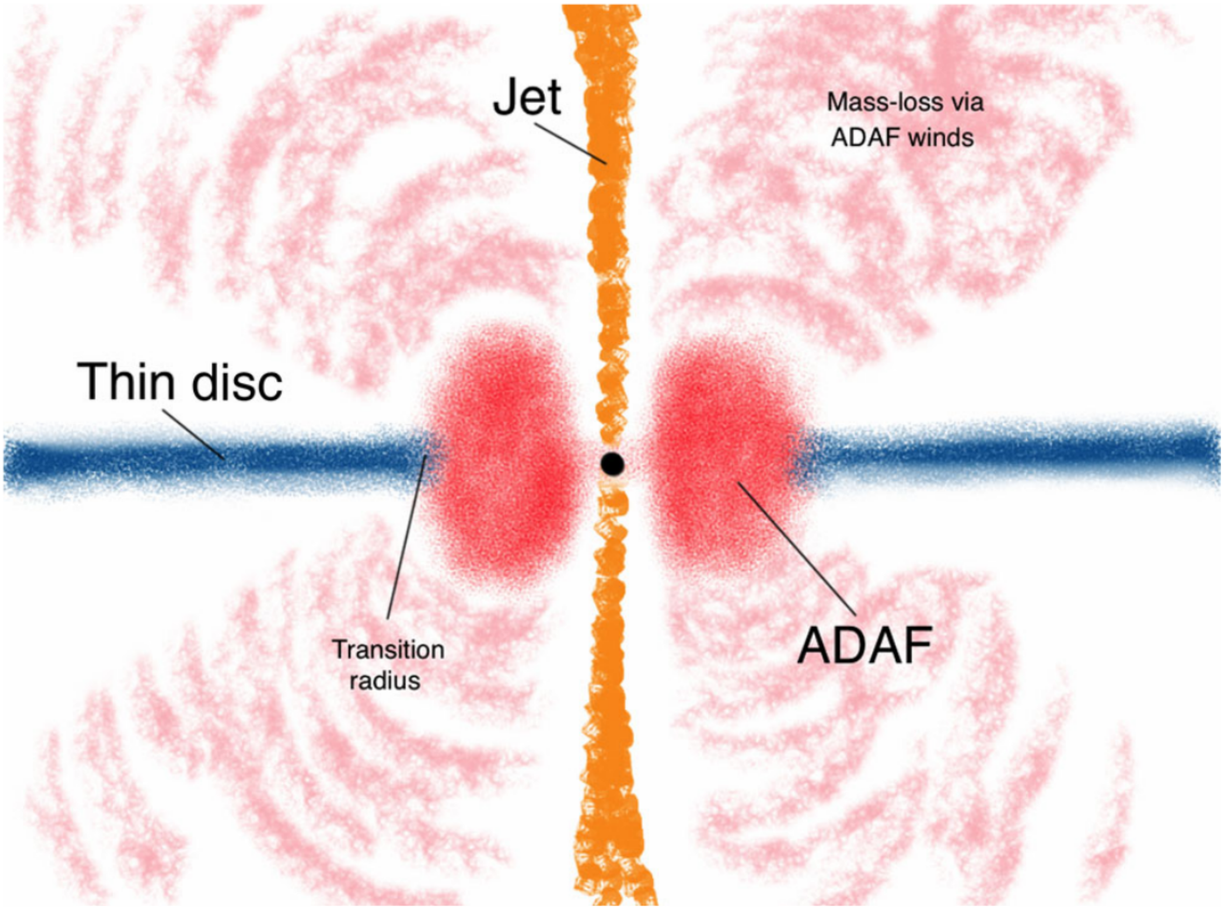

Figure 1.3: Cartoon representing the LLAGN system from Nemmen et al. (2014). In the center an accretion flow in ADAF mode, the target of our simulations. There is other features like jet and an external thin disc in the system that were not contemplated in our work. Our main focus was in investigate the ADAF winds.

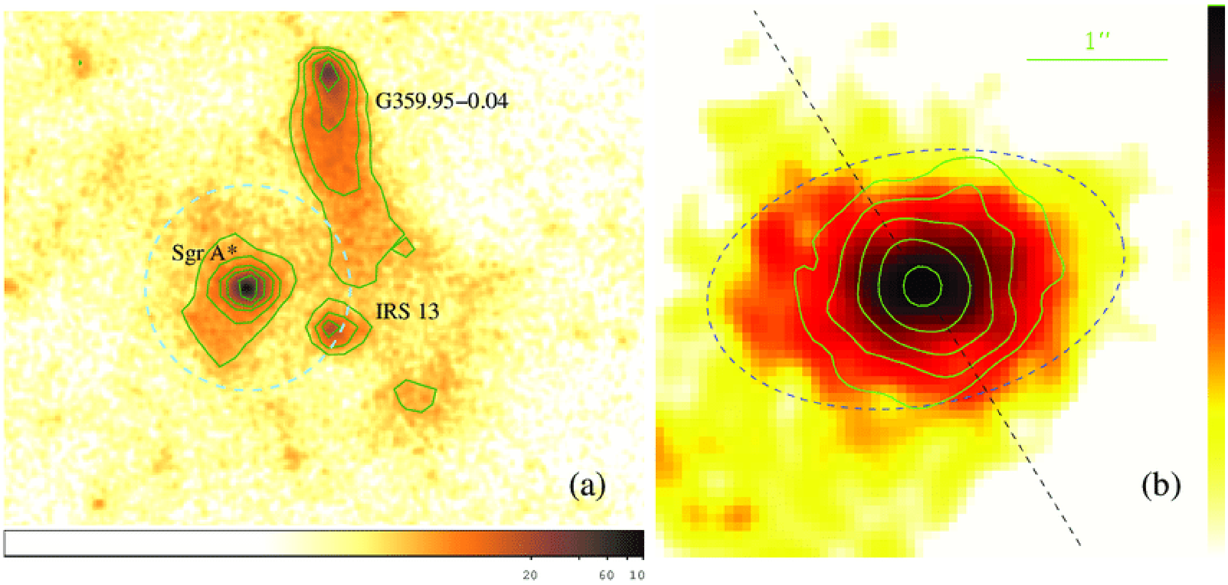

Figure 1.4: SgrA* region in x-rays. Figure extracted from Wang et al. (2013). The left panel is the x-ray observation of the central region of Our Galaxy; the right panel is the zoom into the SgrA* region.

was much higher in the past (Ponti et al., 2010). The bolometric luminosity of the source is $L_{\rm SgrA^*} \approx 10^{36}$erg/s. The accretion flow around SgrA* should be currently in RIAF state and this source is a very good astrophysical laboratory to study hot accretion flows. The spectral energy distribution (SED) of SgrA* is presented in figure 1.5, the emission is dominated by synchrotron emission with peak in submm wavelengths, this emission come from the electronic population of the disc, which is most a thermal population, with a small fraction of non-thermal electrons, with characteristic temperatures of 5-20 MeV (Yuan et al., 2003). In higher energies the main emission come from inverse Compton of the synchrotron photons in the mildly relativistic electrons of the disc.

The second reason is that the existence of a SMBH accreting in a RIAF mode can have important feedback effects in its host galaxy, since RIAFs are quite efficient at producing powerful outflows and jets, as suggested by theoretical studies including analytical calculations (Narayan and Yi, 1994; Blandford and Begelman, 1999; Nemmen et al., 2007; Begelman, 2012) and numerical simulations (e.g., Tchekhovskoy et al. 2011; Yuan et al. 2012; Sądowski et al. 2013; Bu et al. 2016). This is in line with the different observational studies that demonstrate that LLAGNs are generally radio-loud (Nagar et al., 2000, 2001; Ho, 2002; Younes et al., 2012) and accompanied by powerful jets (e.g., Heinz et al. 2007; Merloni and Heinz 2008). Therefore, properly modeling RIAFs and their outflows is relevant to the understanding of AGN feedback.

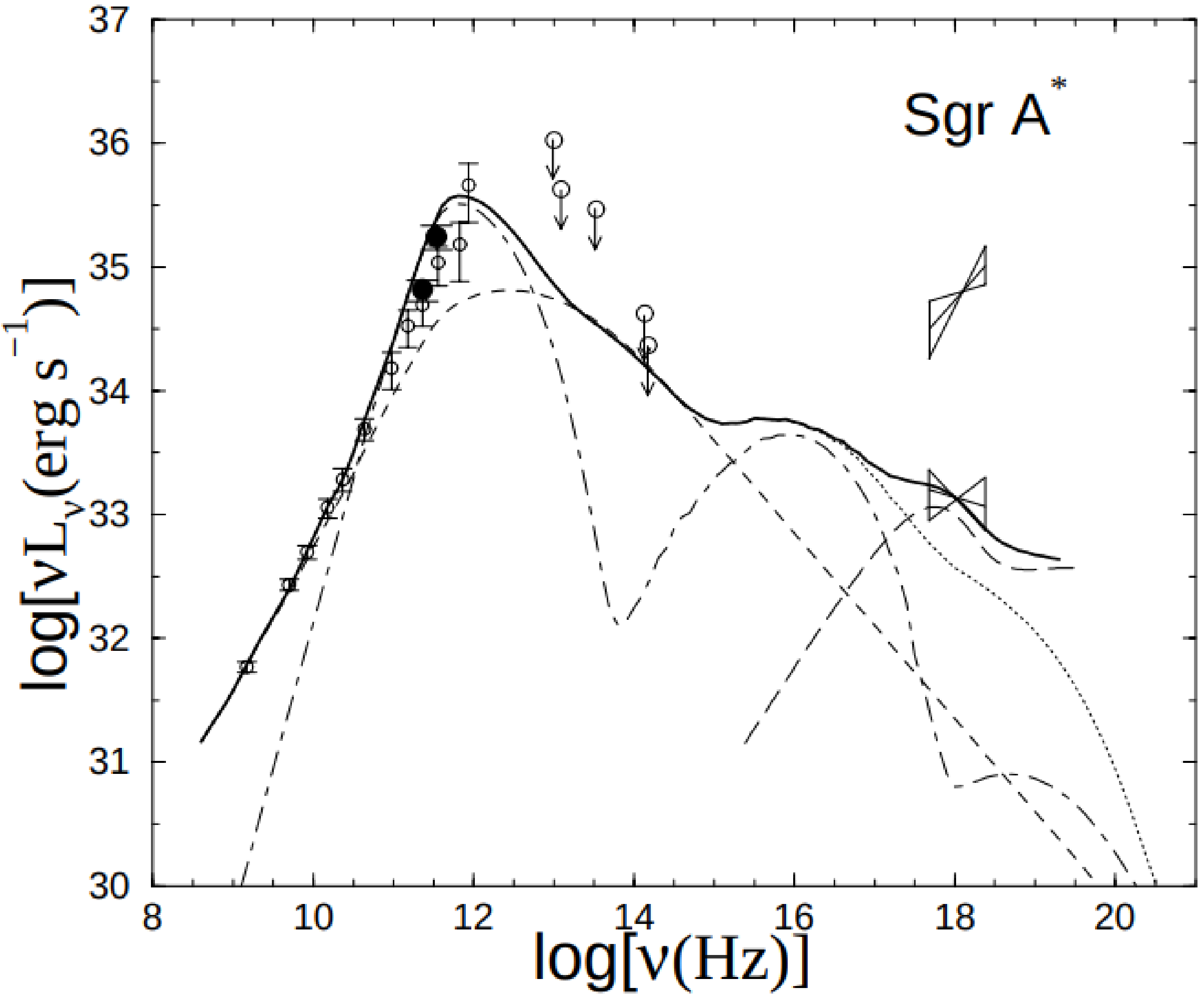

Figure 1.5: SED of SgrA* extracted from Yuan et al. (2003). The solid line is the fit for the quiescent mode, which considered an ADAF scenario dominated by a thermal population of hot electrons, with a small fraction of nonthermal electrons. The dot-dashed line is the synchrotron and inverse Compton emission by thermal electrons; the dashed line is the synchrotron emission by nonthermal electrons; The dotted line is the total synchrotron and inverse Compton emission (thermal and nonthermal); The long-dashed line is the bremsstrahlung emission from the outer parts of the RIAF; The solid line is the sum of all the components.

In fact, it has been proposed that outflows from SMBHs accreting at low rates may be responsible for quenching star formation (Croton et al., 2006; Bower et al., 2006, 2017) and therefore explain the increase in the number of quiescent galaxies–the vast majority of galaxies which have little or no ongoing star formation–over the past ten billion years (Bell et al., 2004; Bundy et al., 2006; Faber et al., 2007; Ilbert et al., 2010). In the centers of galaxy clusters, this kind of feedback is directly observed to be operating and has been called "radio mode"–the action of powerful radio jets launched by the central radio galaxy, which hosts a SMBH accreting at low $\dot{M}$ (Bîrzan et al., 2004), and heat the cluster atmospheres and offset cooling, therefore quenching star formation (McNamara and Nulsen, 2012). There is also evidence for feedback operating in individual galaxies in the form of centrally driven winds from SMBHs in LLAGNs lacking obvious extended radio jets, dubbed "red geysers"; these winds carry out enough mechanical energy to heat ambient, cooler gas and thereby suppress star formation (Cheung et al., 2016; Roy et al., 2018).

The prototype of these red geysers is the galaxy, informally named, Akira studied in Cheung et al. (2016). The ionized gas in the interior of this galaxy presented a velocity excess, the velocity map of Akira is in the left side of figure 1.6. This measured velocities can not be explained only by gravitational effects as it was showed in the right side of figure 1.6. The model to explain these observations is a conic subrelativistic and non-collimated outflow from the center of the galaxy, a scenario very coherent with winds from the region of the SMBH, which is expected for RIAFs.

Moving on closer to home, a major surprise from the *Fermi* Large Area Telescope was the detection of previously unknown giant structures in our Own Galaxy–the so-called Fermi bubbles– above and below the direction of the galactic center (Su et al., 2010; Ackermann et al., 2014). The bubble edges are relatively sharp, transitioning over less than 10° on the sky, which suggests an origin in a particular event rather than a long-term diffusion process. One possibility is that the SMBH at the center of the Milky Way may once have had a stronger activity at its nucleus like that of an AGN, producing powerful outflows within the past few million years (Guo and Mathews, 2012). In figure 1.7 there is the residual map of the sky for high-energy emission excluding the Galaxy and known point sources, the bubbles appears as big structures symmetric in relation to the galactic plane.

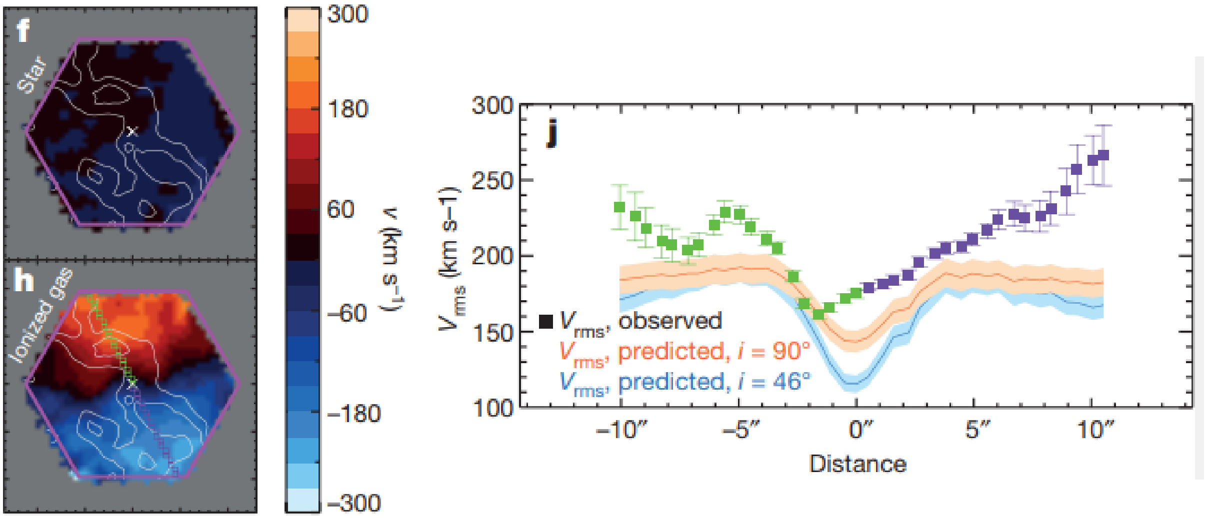

Figure 1.6: Observations of Akira, extracted from Cheung et al. (2016). Left side: map velocities of the stars (top) and the ionized gas(bottom), the contour lines are the map of HII related to the gas. Right side: Models of the expected velocity considering only gravitational effects and inclination in cyan and pink and the data points in green and blue showing a velocity excess.

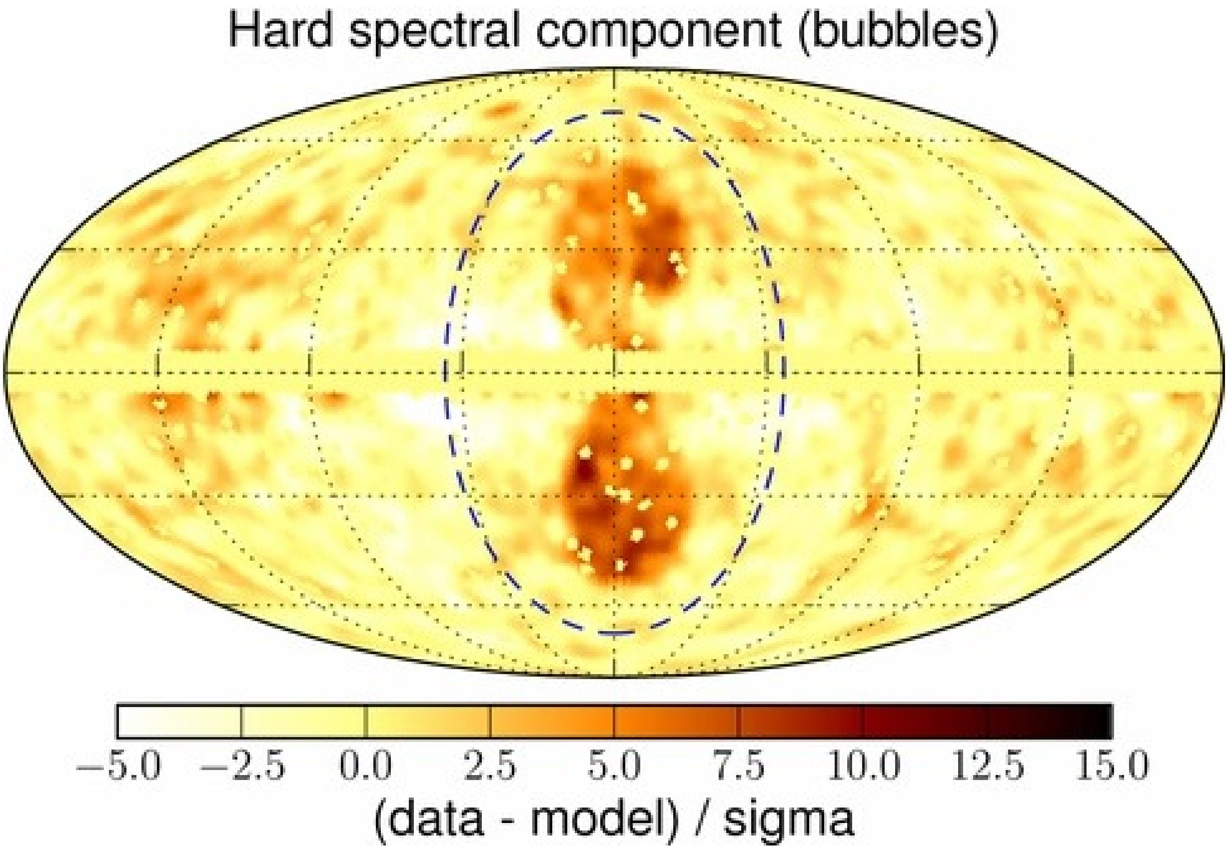

Figure 1.7: Image of the Fermi bubbles extracted from Ackermann et al. (2014). This is a residual plot from the high-energy emission, excluding the galaxy the bubbles have appeared.

1.3 Winds and feedback

An unresolved question is the nature of winds from SMBHs accreting in the RIAF mode in quiescent galaxies: how can these underfed SMBHs produce such powerful winds carrying so much energy and momentum that they heat up gas, shut down star formation and therefore impact the evolution of galaxies–and potentially galaxy clusters? More specifically, what are the energy, momentum and mass outflow rates from such systems? What is the collimation and power of the resulting outflows? Does it provide significant feedback inside the host galaxy? These are the main broad questions that this work will address.

While analytical one-dimensional models are very useful, some aspects of accretion physics such as the formation of outflows and their nonlinear dynamics are beyond the scope of such models. This prompted this work, which employs numerical simulations for studying the global, multidimensional physics of hot accretion flows. More specifically, here we perform global, multidimensional hydrodynamical simulations of RIAFs around BHs, with the goal of investigating in a self-consistent way the winds produced by accreting SMBHs such as those that inhabit the centers of nearby galaxies, and the possible feedback effects in their environment. Since we wanted to keep the simulation conditions as general as possible, we considered only a Schwarzschild BH and did not assume initial conditions with particular magnetic topologies (such as e.g. Narayan et al. 2012), keeping the simulation purely hydrodynamic. Because the BHs in our models are not spinning, we will not have energy extraction from Kerr space-time and hence no Blandford-Znajek driven, Poynting-flux-dominated polar jets (Blandford and Znajek, 1977). This is by design, since we know that jets occur in only ≈ 10% of AGNs (Kellermann et al., 1989)–therefore they cannot account for AGN feedback in the vast majority of quiescent galaxies–and they are also collimated and therefore may not interact efficiently with the interstellar medium.

Technically, the novelty of this work compared to the previous body of numerical simulations of hot accretion flows in the literature is the following: (i) some of our models are the longest running simulations of RIAFs so far produced, with duration of up to $800000GM/c^3$; (ii) our models have a large dynamical range, with the initial outer edge of the torus extending to $500R_S$; (iii) we explored a different prescription for viscous stress tensor based on general relativistic magnetohydrodynamics (GRMHD) global simulations

(Penna et al., 2013); (iv) in some of our models, we adopted the equilibrium torus solution of Penna et al. (2013), which corresponds to a more physical initial condition than earlier torus solutions; (v) finally, we adopted a Lagrangian tracer particles to improve the estimates of quantities associated with the outflows.

The structure of this work is as follows. In section 2.2 we outline the computational methods used to solve the fluid conservation equations, initial conditions, parameter space and techniques used in the analysis. In section 3 we describe the results: the temporal evolution of the flow, amount of energy, momentum and mass outflow rates, geometry, collimation and launching radii of winds, and the density profile of the accretion flow. In section 4.1 we contextualize our results, comparing our simulated accretion flows and outflows with observations of LLAGNs and AGN feedback, and also with previous numerical models. Finally, we conclude with a summary and perspectives in section 4.2.

Readers interested in the density profiles of the hot accretion flow can skip to section 3.1. Those interested in the outflow properties and feedback efficiency should go to sections 3.1.2, 3.2. The comparisons with observations of LLAGNs, SgrA* and AGN feedback can be found in section 4.1.

Chapter 2

Methods

In this work, we aim at simulating the evolution of thick accretion flows around black holes. We are particularly interested in understanding the origin and development of subrelativistic winds from black holes, for which the extraction of spin energy from the black hole is thought to be not so important–as opposed to relativistic jets. For this reason, we considered only a Schwarzschild black hole and adopted a Newtonian hydrodynamical (HD) treatment, describing the black hole gravity in terms of the pseudo Newtonian potential (Paczyńsky and Wiita 1980; cf. section 2.1).

We performed our numerical simulations with the `PLUTO` code We did not take into account electromagnetic fields explicitly; instead, we incorporated the energy and angular momentum dissipation expected due to the magnetorotational instability (MRI; Balbus and Hawley 1998) by means of an appropriate viscous stress tensor (cf. section 2.1).

2.1 Equations set

The set of equations describing hydrodynamic accretion flows were presented in Stone et al. (1999); these equations are reproduced below:

$$\frac{d\rho}{dt} + \rho\nabla\cdot\mathbf{v} = 0, \tag{2.1}$$

$$\rho\frac{d\mathbf{v}}{dt} = \nabla P - \rho\nabla\psi + \nabla\cdot\mathbf{T}, \tag{2.2}$$

$$\rho\frac{d\mathbf{e}/\rho}{dt} = -P\nabla\cdot\mathbf{v} + \frac{\mathbf{T}^2}{\mu}. \tag{2.3}$$

In equations (2.1) - (2.3), ρ is the density, $\mathbf{v}$ is the velocity, P is the pressure, e is the internal energy density, ψ is the gravitational potential and $\mathbf{T}$ is the anomalous stress tensor. We adopted the pseudo Newtonian potential $\psi = GM/(R - R_S)$ which incorporates the basic features of the Schwarzschild geometry (Paczyńsky and Wiita, 1980).

In a more complex scenario, considering magnetic fields, we expected stresses due to magnetohydrodynamic turbulence driven by the MRI (Balbus and Hawley, 1998). In our case, however, our setup was fully hydrodynamic, hence in order to implement angular momentum transport we need to introduce some approximations. In order to incorporate angular momentum transport that mimics MRI, we followed Stone et al. (1999) and assumed that the non-azimuthal components of **T** are zero; the non-zero terms of **T** are, in spherical-polar coordinates (R, θ, ϕ):

$$T_{R\phi} = \mu R \frac{\partial}{\partial R}\left(\frac{v_\phi}{R}\right), \tag{2.4}$$

$$T_{\theta\phi} = \frac{\mu \sin\theta}{R}\frac{\partial}{\partial \theta}\left(\frac{v_\phi}{\sin\theta}\right), \tag{2.5}$$

where $\mu = \nu\rho$ is the viscosity coefficient and ν is the kinematic viscosity (Landau and Lifshitz, 1959). In this work we explored two different prescriptions for the viscous stress by adopting different parameterizations for ν:

1. $\nu = \alpha r^{1/2}$ which corresponds to the “K-model” in Stone et al. (1999). We will refer to this ν-scaling as ST.
2. $\nu = \alpha c_s^2/\Omega_K$ following Shakura and Sunyaev (1973). We will refer to this parameterization as SS.

In the above expressions, Ω_K is the Keplerian angular velocity and c_s is sound speed. The α parameter is the usual Shakura-Sunyaev α-parameter for accretion discs (Shakura and Sunyaev, 1973) which we allow to vary in the range $0.01 \leq \alpha \leq 0.3$. Note that, strictly speaking, the α here corresponds exactly to the “Shakura-Sunyaev α” only in the SS model.

We also explored a model in which α varies with radius, i.e. $\alpha = \alpha(R)$, inspired on Penna et al. (2013). Penna et al. obtained an analytical approximation to $\alpha(R)$ that reproduces well the numerical GRMHD simulations of RIAFs, which we reproduce here:

$$\alpha(R) = \begin{cases} \frac{1}{40}\left(\frac{1-\frac{1}{R}}{1-\frac{1.5}{R}}\right)^6, & R > 3R_S \\ 0.140466, & R < 3R_S \end{cases}. \tag{2.6}$$

2.2 PLUTO

2.2.1 Mathematical methods

The simulations performed here were done with the `PLUTO` code (Mignone et al., 2007), which solves the fluid conservation equations with an emphasis on astrophysical applications. `PLUTO` can perform fluid simulations in 1, 2 or 3 dimensions, considering different types of coordinates. The code has different modules that handle equations of hydrodynamics (HD) and magnetohydrodynamics (MHD), both in classic or special relativistic scenarios. `PLUTO` was particularly developed to treat astrophysical flows with discontinuities, (e.g. shocks). The code was designed to integrate, in a discrete grid, a system of conservation laws –these laws are not obligated to have physical meaning– using Godunov-type shock capturing schemes.

The code was built to integrate a generic system with the form

$$\frac{\partial \mathbf{U}}{\partial t} = -\nabla \cdot \mathbf{T}(\mathbf{U}) + \mathbf{S}(\mathbf{U}), \tag{2.7}$$

$\mathbf{U}$ is the vector that represents the conserved quantities; $\mathbf{T}(\mathbf{U})$ is a rank 2 tensor, its rows represent the fluxes of the conserved quantities; $\mathbf{S}$ are called the source terms, external fields (e.g. gravitational potential) are added here.

The conserved variables, in a physical hydrodynamical system should be the density ρ, the linear momentum $\mathbf{p} = m\mathbf{v}$ and the energy E. These variables are not the easiest ones to make the calculations, so the code works with a different set of variables called primitive variables, denoted as $\mathbf{V}$. These variables, for the cited case, can be ρ, $\mathbf{p}$ and the pressure p, this choice transformation $\mathbf{U} \to \mathbf{V}$ can be beneficial to set constrains like $p > 0$ or subluminal speeds.

We extracted the figure 1 from Mignone et al. (2007) and showed it in figure 2.1, this is the fluxogram of `PLUTO` tasks. First there is the conversion between the conserved variables to primitives variables; second, the code finds the values of the primitive variables in the numerical cell edges; third, the code solves the Riemann problem at the edges of the cells; after all this, the new temporal state is calculated (Toro, 2013).

Most part of mechanics equations are hyperbolic, same for fluid equations (e.g. wave equation). Hyperbolic equations can be defined as a partial differential equations system in that the Cauchy problem can be locally solved for any initial data along any non-

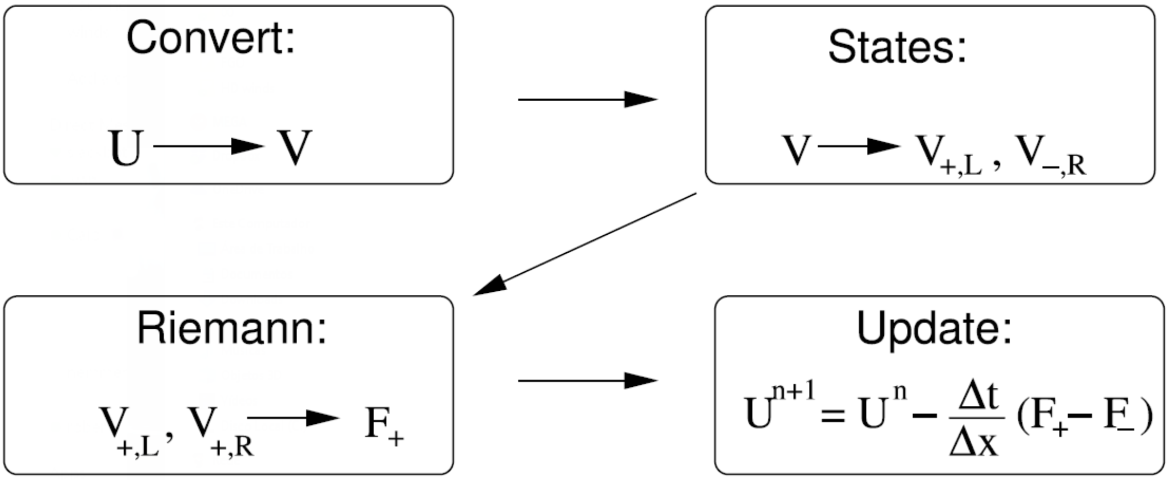

Figure 2.1: Image extracted from Mignone et al. (2007), this is the fluxogram of the numerical processes in `PLUTO`.

characteristic surface (hyp, 2019). In practice, they are roughly a well-posed initial value problem. `PLUTO` uses a Godunov-type method to solve the set of hyperbolic equations for the flow. van Leer (1997) gave the succinct definition for Godunov methods:

> ”*... we define Godunov-type methods as non-oscillatory finite-volume schemes that incorporate the solution (exact or approximate) to Riemann's initial-value problem, or a generalization of it,...*”

`PLUTO` works with the discretization of the variables in space and time (in both approaches, classic or relativistic), it adopts the finite volume method. In each cell there is a volume average of the variables, for a one-dimensional case, of one cell in a discretized grid, with edges in $x_{i\pm1/2}$ the value of the primitive variables in the cell will be:

$$\mathbf{V}_i^n = \frac{1}{x_{i+1/2} - x_{i-1/2}} \int_{x_{i-1/2}}^{x_{i+1/2}} \mathbf{V}(x, t_n) dx. \tag{2.8}$$

Properly, the finite volume method is a n-dimensional expansion of the idea from (2.8).

In the second step of figure 2.1, `PLUTO` executes a polynomial reconstruction that respects monotonicity inside the cells. For each cell, we have a boundary surface that is shared with the neighbour cell. For an one dimensional case, the cell has two boundaries (we denoted as x_- and x_+), and a distribution inside the cell, this distribution is defined by a polynomial approximation $\mathbf{P}(x)$, which is centered around the value calculated in (2.8). After the polynomial reconstruction, the primitive variables will present value in the two boundaries $\mathbf{V}_+$ and $\mathbf{V}_-$ obeying:

$$\mathbf{V}_{\pm} = \lim_{x \to x_{\pm}} \mathbf{P}(x). \tag{2.9}$$

If `PLUTO` did not make the interpolation and assume that the variable is homogeneous inside the whole cell volume, it leads to higher numerical errors, because the discontinuities would become steeper.

For a pair of neighbour cells –let us call them as cells A and B–, they share a boundary surface and each cell had their own values for $\mathbf{V}_{\pm}$ in the shared edge. In the boundary surface, cell A had the value $\mathbf{V}_+^A$ and cell B had the value $\mathbf{V}_-^B$, these two values are not the same, they both depended on the average value of $\mathbf{V}$ in each cell and the interpolation process (2.9). In the whole grid we have discontinuities like that and these discontinuities can not be neglected in the fluid evolution. This scenario of discontinuity evolution is called the Riemann problem and it should be solved in the numerical code. `PLUTO` has options of Riemann solvers in its build (e.g HLL, HLLC, ROE), for the complete list see the `PLUTO` user's guide available in `http://plutocode.ph.unito.it/documentation.html`. With these methods, `PLUTO` are able to compute the numerical flux functions related to the $\mathbf{T}(\mathbf{U})$ term of (2.7).

The forth, and last, step presented in figure 2.1 is the temporal evolution of the variables $\mathbf{U}_i^n \to \mathbf{U}_i^{n+1}$. `PLUTO` calculate this from the fluxes generated in the Riemann solver step as it follows:

$$\frac{d\mathbf{U}}{dt} = \mathbf{L}^n, \tag{2.10}$$

the time derivative was calculated using a 2$^{\text{nd}}$ order Runge-Kutta method, the time step is calculated depending of numerical parameters present in the third step (Courant et al., 1928) and $\mathbf{L}^n$ is an operator that carries the flux differences in the cell,

$$\mathbf{L}^n = -\frac{1}{\delta\Lambda}\left(A_+^n \mathbf{F}_+^n - A_-^n \mathbf{F}_-^n\right) + \mathbf{S}^n. \tag{2.11}$$

$+$ and $-$ refer to the edges of the cell, A is the respective area of the edge and $\mathbf{F}$ the flux across that area; $\delta\Lambda$ is the cell volume. The first term of the right-hand side is the net density of the variable in the cell. The source term $\mathbf{S}$ is added here as an external agent. `PLUTO` has some methods, with different orders to perform (2.10), more details can be seen in Mignone et al. (2007); Toro (2013).

2.2.2 Hydrodynamic module

In this work we used only the hydrodynamic module of `PLUTO`. This mode implements the equations for a fluid in the classical sense coupled with a defined equation of state. The variables are the traditional:

$$\mathbf{U} = (\rho, \rho\mathbf{v}, E)^T \, ; \qquad \mathbf{T}(\mathbf{U}) = (\rho\mathbf{v}, (\rho\mathbf{v})\mathbf{v} + p\mathbf{I}, (E+p)\mathbf{v}) \, , \tag{2.12}$$

where, $\mathbf{I}$ is the unitary matrix and all the variables were defined in the beginning of the section.

The source terms ($\mathbf{S}$) that we used were an external gravitational potential and viscosity. Gravitational potential is a local source term that depends only of the variables, and not from their derivatives so it is more easily handled by the code than the viscosity, which is a non-ideal effect that introduces parabolic corrections and require the solution of diffusion equations (Mignone et al., 2007). `PLUTO` had modules that can treat these source terms in its original building, there was no need to adapt any block of the main code in order to perform our simulations.

2.3 Computational method

We adopted units such that $GM = 1$ and the Schwarzschild radius is unitary, $R_S \equiv 2GM/c^2 = 1$ (i.e. $c = \sqrt{2}$). Length and time in this paper are given in units of $2GM/c^2$ and GM/c^3, respectively.

Our simulations run for a very long time, since we are interested in the *global* dynamics of the accretion flow and winds. We can make a rough estimate of the simulation duration necessary for the flow state to converge. The basic idea is that we expect the flow to reach a steady state equilibrium on a timescale comparable to the viscous time $t_{\rm visc}$. The simple self-similar ADAF model (Narayan and Yi, 1994) gives us useful scaling, according to which the viscous time at a radius R is given by

$$t_{\rm visc} = \frac{R}{v_R} \sim \frac{t_{\rm ff}}{0.5\alpha} \tag{2.13}$$

where α is the Shakura-Sunyaev viscosity parameter and $t_{\rm ff}$ is the free-fall timescale. This simple model indicates that in order for a parcel of gas located at $R = 500R_S$ in the disk to achieve inflow equilibrium, it would take an amount of time $t \sim t_{\rm visc} = 200000GM/c^3$

for $\alpha = 0.3$. Therefore, our simulations need to have a comparable duration in order to ensure that the flow achieves convergence in at least part of the domain, thus justifying the long running times. The running time of the simulations varied between 40000 to $800000 GM/c^3$, depending on whether we found a specific simulation to be more promising in terms of its potential for wind launching potential.

Our black hole accretion flow simulations have the longest duration to date, to our knowledge. The long duration of our models imply that they are usually quite computationally expensive. For this reason, we have chosen to restrict the dimensionality of our models to only two dimensions.

2.4 Initial conditions and grid

Our initial condition consists of a rotating HD torus in dynamical equilibrium with a specific angular momentum profile $l(r)$. The torus' inner edge is located at $R_{\rm in} = 5 - 20 R_S$ – the variation was due to numerical reasons and was dependent of the change of $l(r)$ – and outer edge $R_{\rm out} \approx 500 R_S$. The radius of maximum density R_0 was varied in our models in the range $R_0 \approx 10 - 25 R_S$ depending on the $l(r)$ model adopted, bound by the values of $R_{\rm in}$ and $R_{\rm out}$. Our torus is pretty large–larger than most simulations which usually begin with a torus ending at $\approx 40 R_S$ (e.g., Mościbrodzka and Falcke 2013; Porth et al. 2017)–since we are interested in both the density profile up to larger scales and whether winds are launched at larger radii from the disk.

We explored two $l(r)$-profiles in our simulations, both depending only on the cylindrical radius r:

1. Power-law scaling $l(r) \propto r^a$, where $0 \leq a < 0.5$. Papaloizou and Pringle (1984) reported a full analysis of the $a = 0$ case. Here, considered three different values of a: 0.0, 0.2 and 0.4.

2. $l(r)$ piecewise scaling proposed by Penna et al. (2013), adapted to a non-relativistic torus: $l =$ constant for $r < 21 R_S$, $l(r) = 0.71 l_K$ elsewhere where l_K is the Keplerian specific angular momentum.

The four torus described above are shown in Figure 2.6. As can be seen in this figure, a has the effect of changing the torus thickness. The reason why we explored models with

$a > 0$ is because we wanted to initialize models with a torus thickness $H \sim r$ as expected for RIAF models (Yuan and Narayan, 2014), where H is the scale height.

Regarding the computational domain, we use a fixed mesh and our grid extends to a large radius, $10^4 R_S$–which is one order of magnitude larger than the outer radius of the disc size–in order to avoid undesirable boundary effects. Our grid is uniformly distributed in $\log_{10}$(radius) with 400 cells; as such, the inner regions have a higher resolution. The radius of the computational domain begins at $1.25 R_S$. The boundary conditions adopted were outflow borders in the radial component and axyssimetric reflective borders in the azimuthal component, in order to represent a 3D spherical scenario.

To avoid numerical errors, the grid is restricted to $2° \leq \theta \leq 178°$. In the θ-direction, we defined two regions with a different number of cells in each, such that we have less cells near the grid poles (Figure 2.7). The regions are separated according to the values of θ:

$$N_{\text{cells}} \text{ in } \theta\text{−direction} = \begin{cases} 10, & \text{if } \theta < 15° \text{ or } \theta > 165° \\ 180, & \text{if } 15° \leq \theta \leq 165° \end{cases} . \tag{2.14}$$

The reason why we decreased the spatial resolution near the poles is because we do not expect any significant action to occur in this region. Therefore we have chosen to concentrate the resolution in the equatorial regions where we expect the development of the accretion flow and wind. If we were simulating the flow around a Kerr BH, then we would expect to have a Poynting flux-dominated jet which would fill the polar regions. However, since we are dealing with a Schwarzschild black hole, our grid choice is appropriate.

2.5 Lagrangian particle tracking

One technique that we used to identify and characterize outflows–in addition to analyzing the evolution of the mass and energy fluxes across our mesh-based simulations–was to introduce "tracer" particles which are be passively advected with the fluid flow, and thereby track its Lagrangian evolution, allowing the thermodynamic history of individual fluid elements to be recorded. This technique is called Lagrangian particle tracking and has been used to make sense of several astrophysical simulations (e.g. Enßlin and Brüggen 2002; Dubois et al. 2012; Genel et al. 2013; Yuan et al. 2015). It is particularly useful in our simulations, since it does not rely on using the Bernoulli parameter which is an indi-

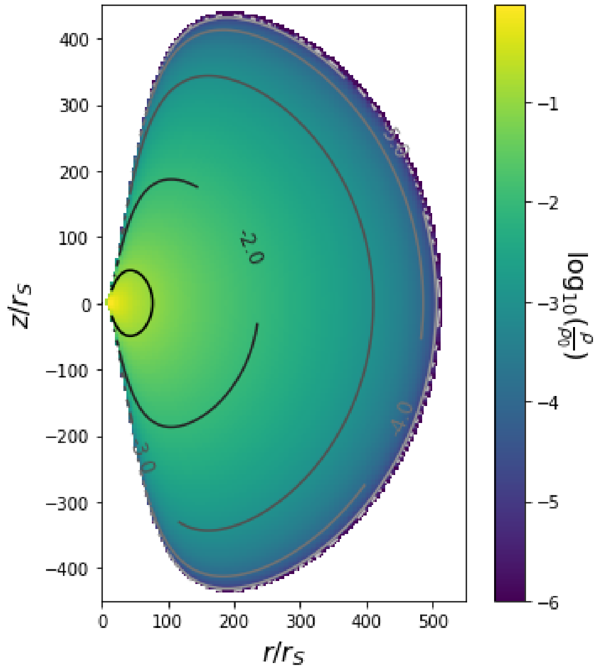

Figure 2.2: $l(r)$ = constant

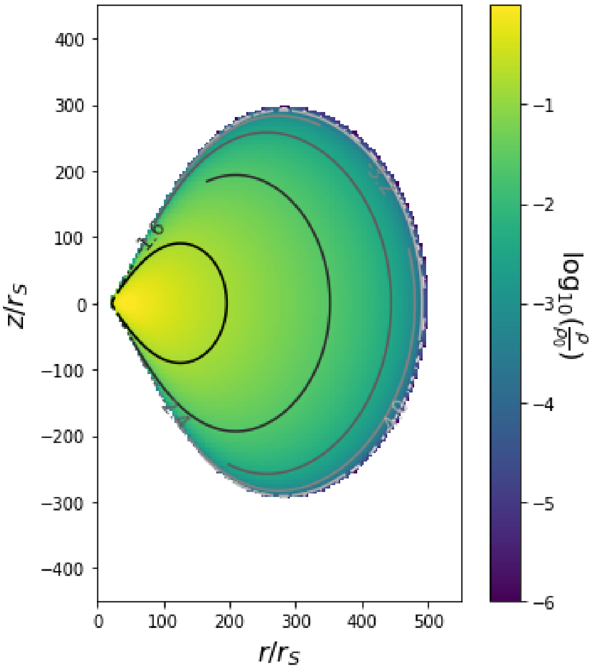

Figure 2.3: $l(r) \propto r^{0.2}$

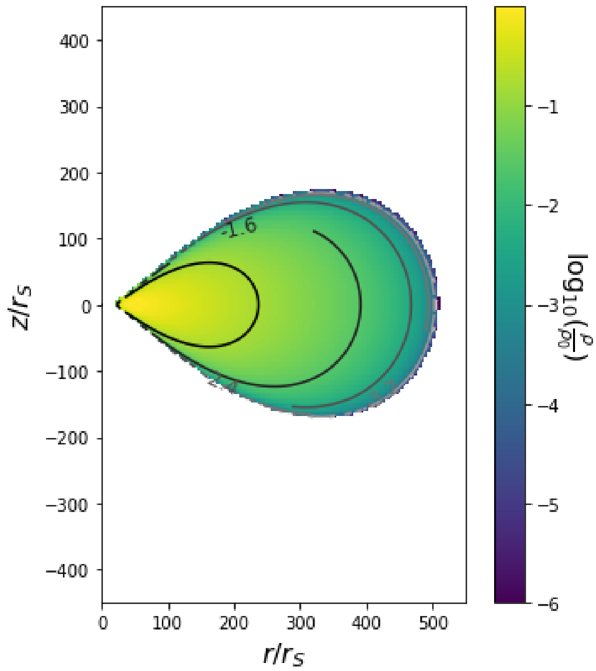

Figure 2.4: $l(r) \propto r^{0.4}$

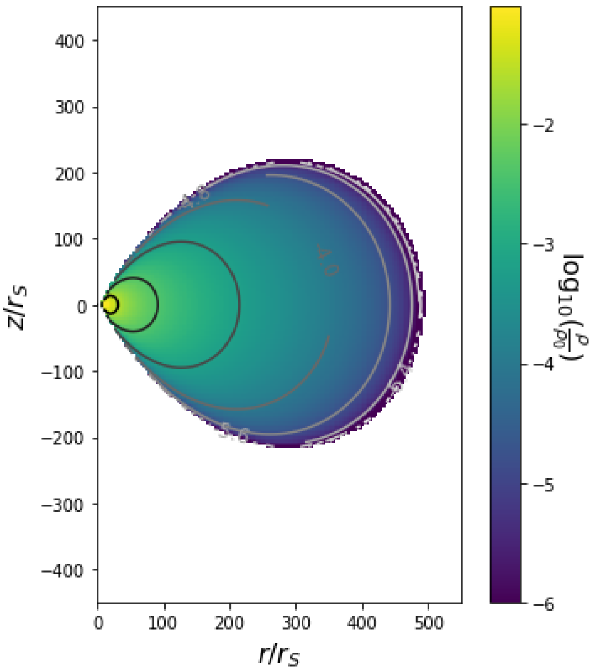

Figure 2.5: $l(r)$ inspired on Penna et al. (2013)

Figure 2.6: Torus density distribution for the four specific angular momentum profiles considered.

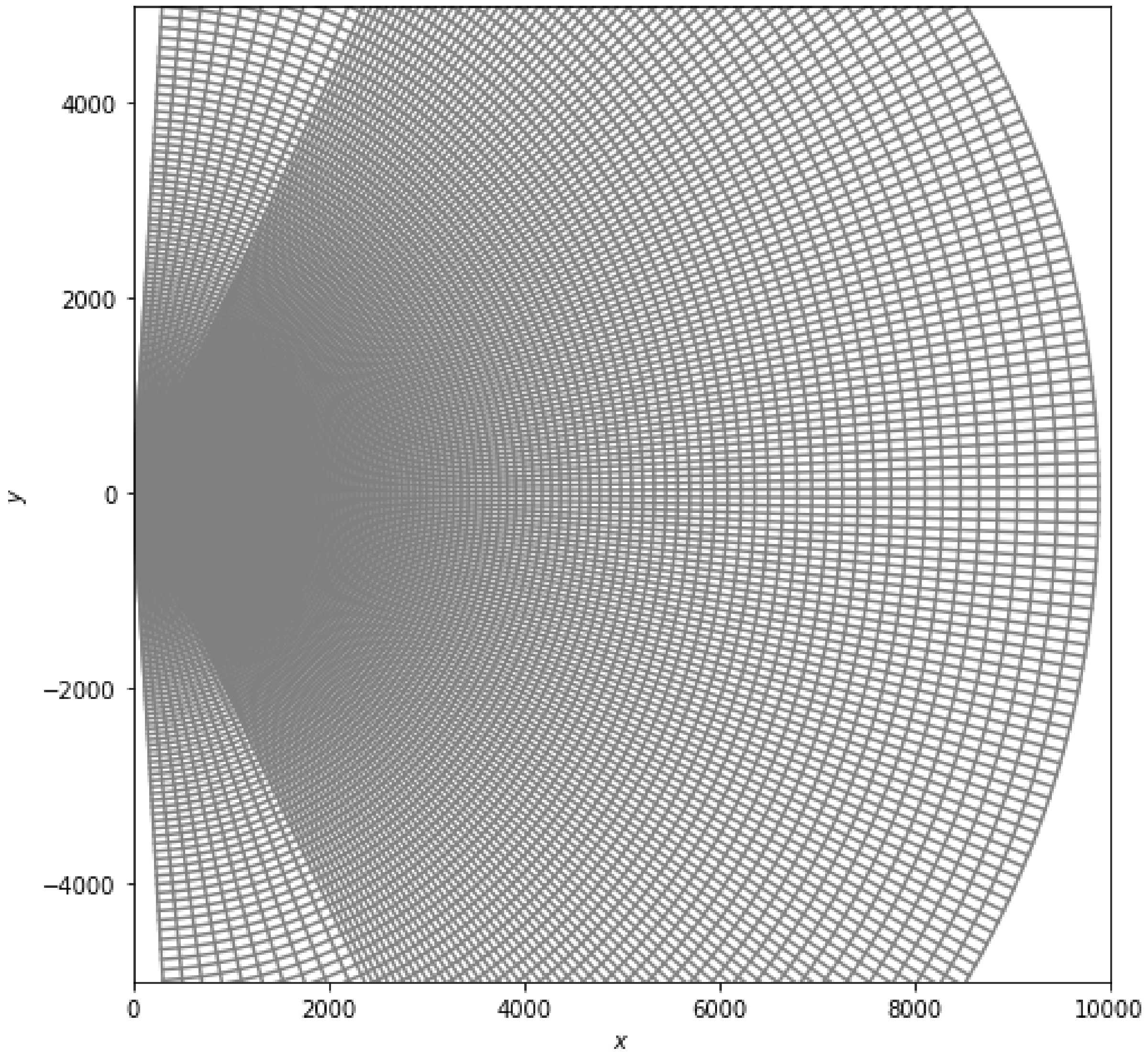

Figure 2.7: Grid used in the simulations.

rect way of assessing whether outflows were produced, therefore being a more appropriate outflow measure.

We implemented the traditional scheme in which the tracer particles are massless particles advected in space using the local velocity field (Harlow and Welch, 1965). To obtain the trajectories of the particles, we solve the differential equation

$$\frac{d\mathbf{x_p}}{dt} = \mathbf{v_f}(\mathbf{x_p}, t) \tag{2.15}$$

where $\mathbf{x_p}(t)$ is the particle position and $\mathbf{v}$ is the fluid velocity at the position $\mathbf{x_p}$. With the velocities from simulation data at a particular time t, we can advance the position of the tracer particle to $t + \Delta t$ which is accurate to first-order, limited by the time-resolution of the simulation.

The simulations' time step Δt were chosen to be sufficiently short–approximately the orbital Keplerian period t_K at $R \approx 8R_S$–such that the distance a fluid element is able to cover over a timescale t_K is much smaller than the size of the disc, $v\Delta t \ll R_{\rm out}$ where in this context v is a typical fluid velocity.

In order to assess whether outflows are produced from a given simulation and–in case there is an outflow–to quantify its properties, we used a set of 1250 tracer particles. We started the particle tracking at the moment when the fluid has reached a stationary net mass accretion rate, i.e. when the value of $\dot{M}_{\rm acc}(R_{\rm in}, t)$ (cf. equation 3.1, Figure 3.2) becomes roughly constant; we defined this moment as t_0. The particles are initially uniformly distributed in a region delimited by $R = 40R_S - 150R_S$ and $\theta = 15° - 165°$. For $t > t_0$, we let the particles be advected by the flow and we monitor their positions with time.

In this work we adopted two criteria for identifying whether a tracer particle is part of an outflow. Firstly, since we are only interested in the properties of winds, we reject particles which are located near the poles–the domain of the relativistic if we had a Kerr BH (e.g. Sądowski et al. 2013)–or in the accretion disc. Quantitatively, we only consider particles which by the end of the simulation have $15° \leq \theta \leq 45°$ or $135° \leq \theta \leq 165°$. Secondly, based on the final radius $R_{\rm final}$ of the particle we have defined two types of outflow:

1. If $R_{\rm final} > 500R_S$ we call "real outflow", i.e. the particle reaches a distance larger than the maximum radius of the original torus ($R_{\rm final} > R_{\rm out}$).

2. If $R(t = t_0) < R_{\rm final} < R_{\rm out}$, we call this “simple outflow”, i.e. the particle was not accreted but also did not reach very far away.

Following these two criteria, the “wind region” is illustrated in Figure 2.8; particles that get outside the red circle are presumably part of a wind launched by the black hole.

2.6 Simulation setup

We performed a total of 10 simulations exploring the variation of three main properties of the flow: the specific angular moment profile $l(r)$, the viscosity prescription ν and the value of α; the parameter space of simulations is summarized in Table 2.1 and visually depicted in Figure 2.9. It is important to investigate different $l(r)$-profiles since the actual rotation curve of RIAFs in nature is not known. In particular, we do not know the initial conditions of SMBH accretion in low-luminosity AGNs, and the long-term evolution of the accretion flow and possible winds could be dependent on these initial conditions, which is an incentive to not be too conservative in choosing the parameters of our numerical experiments.

Table 2.1 - List of the numerical simulations performed in this work. The second column refers to the specific angular momentum. ”Penna+13”refers to the torus described in Penna et al. (2013) and the others are related to a power-law form $l(r) \propto r^a$ (see section 2.4); ν and α columns refer to the adopted viscosity profile and the dimensionless coefficient (see 2.1).

#ID	l(r)	ν	α	Duration $\left[\frac{GM}{c^3}\right]$
00	Penna+13	ST	0.01	803641
01	Penna+13	ST	0.1	90283
02	Penna+13	SS	0.1	447061
03	Penna+13	SS	0.3	334009
04	Penna+13	SS	$\alpha(r)$	384496
05	$a = 0.0$	ST	0.1	76028
06	$a = 0.0$	SS	0.3	209077
07	$a = 0.2$	SS	0.1	138395

Continues in the next page…

Tabela 2.1 - Continuation

#ID	l(r)	ν	α	Duration $\left[\frac{GM}{c^3}\right]$
08	$a = 0.2$	SS	0.3	211453
09	$a = 0.2$	ST	0.1	37618
10	$a = 0.4$	ST	0.01	170073

The other two parameters–ν and α–are responsible for the angular momentum transport that allows accretion to proceed. We described the two parameterizations of ν that we adopted in section2.4. We expect the long-term behavior of the flow to strongly depend on the functional form of ν. Moreover, α regulates the strength of the angular momentum removal as in the classical Shakura-Sunyaev solution. We chose values of α consistent with estimates from global and shearbox simulations of the MRI process in BH accretion flows (cf. Penna et al. 2013 for a review).

As argued in section 2.3, we ran the simulations for a long time–comparable to the viscous time at large radii in the disc–in the hopes that a considerable part of the accretion flow converges. On the opposite end, models 02-04 had very high running times $\gtrsim 300000GM/c^3$ and #ID00 had an extreme high running time of $\sim 800000GM/c^3$, which is the longest BH accretion flow simulation produced to date, to our knowledge[1].

The methodology adopted to run the simulations are presented in figure 2.10, this was roughly the step-by-step followed to generate all the data. In the figure there is boxes as "Let it run in the cluster for some days", the number of days was not fixed, each simulation had a different run time and this time is not necessarily proportional to the simulated time in GM/c^3, it depends of numerical factors –the time step for each simulation is different. And in the same picture it is said that we allowed longer runs to "promising simulations"that is simulations in that the torus was not destroyed or fell into the BH, –or any other event that we considered non-physical for our knowledge about accretion flows– the definition of promising was arbitrary.

---

[1] The previous longest-duration simulation is the three-dimensional GRMHD model of a RIAF performed by Chan et al. (2015), which ran for 230990 GM/c^3.

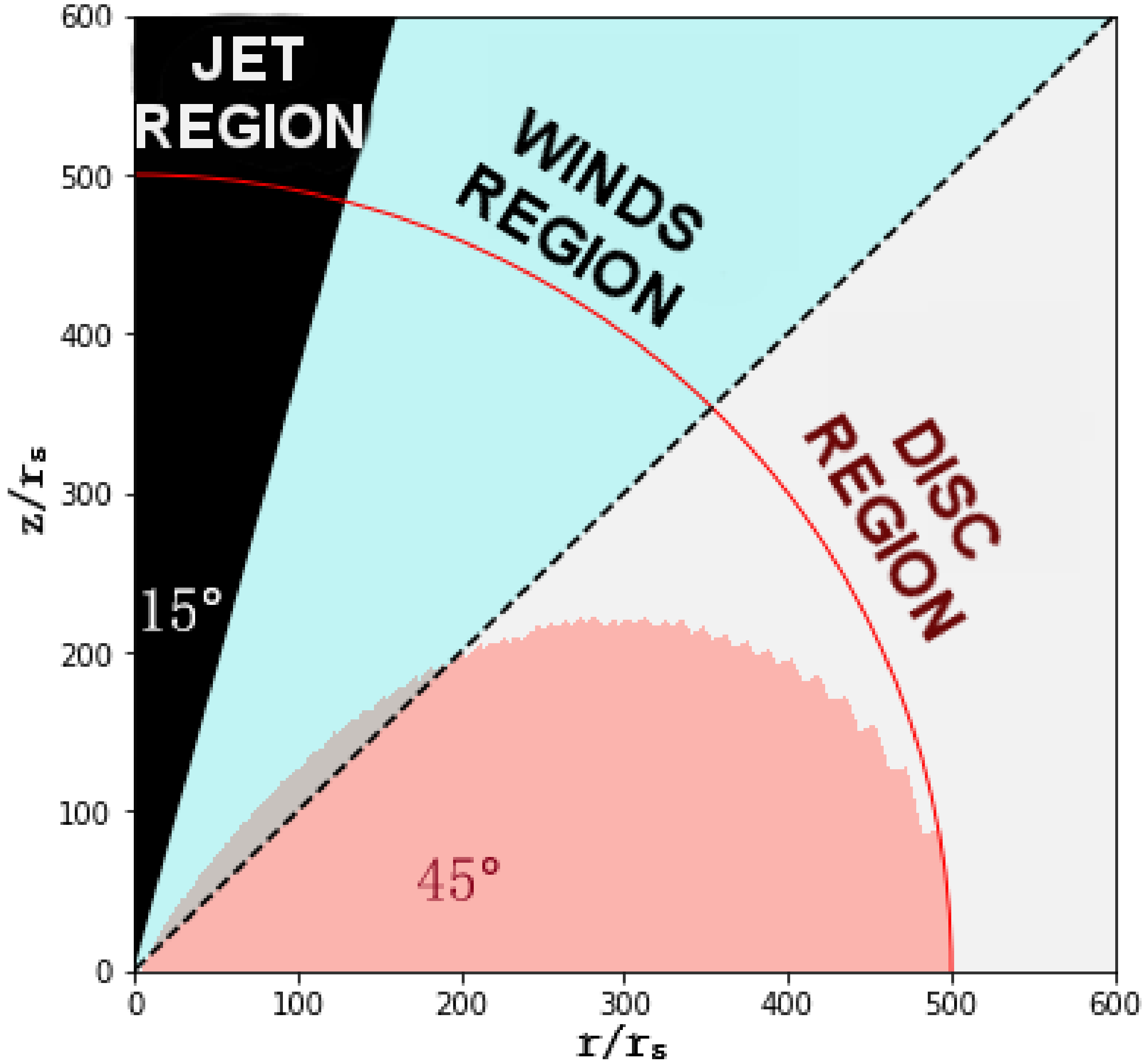

Figure 2.8: Schematic drawing of the different regions of the flow. Jet region are defined as a region near the pole with 15°opening, and the disc region is a region near the equator with 45°opening; all material ejected in these two regions are excluded in our analysis of outflows because this regions are believed to be dominated by jet and accretion disc, respectively, in nature. We considered only the region between both, that we called wind region (WR) and are represented in blue. The red solid line is the outflow limit that we have defined, every material that it is in the wind region and beyond the red line was classified as real outflow. The pink solid region is our initial torus.

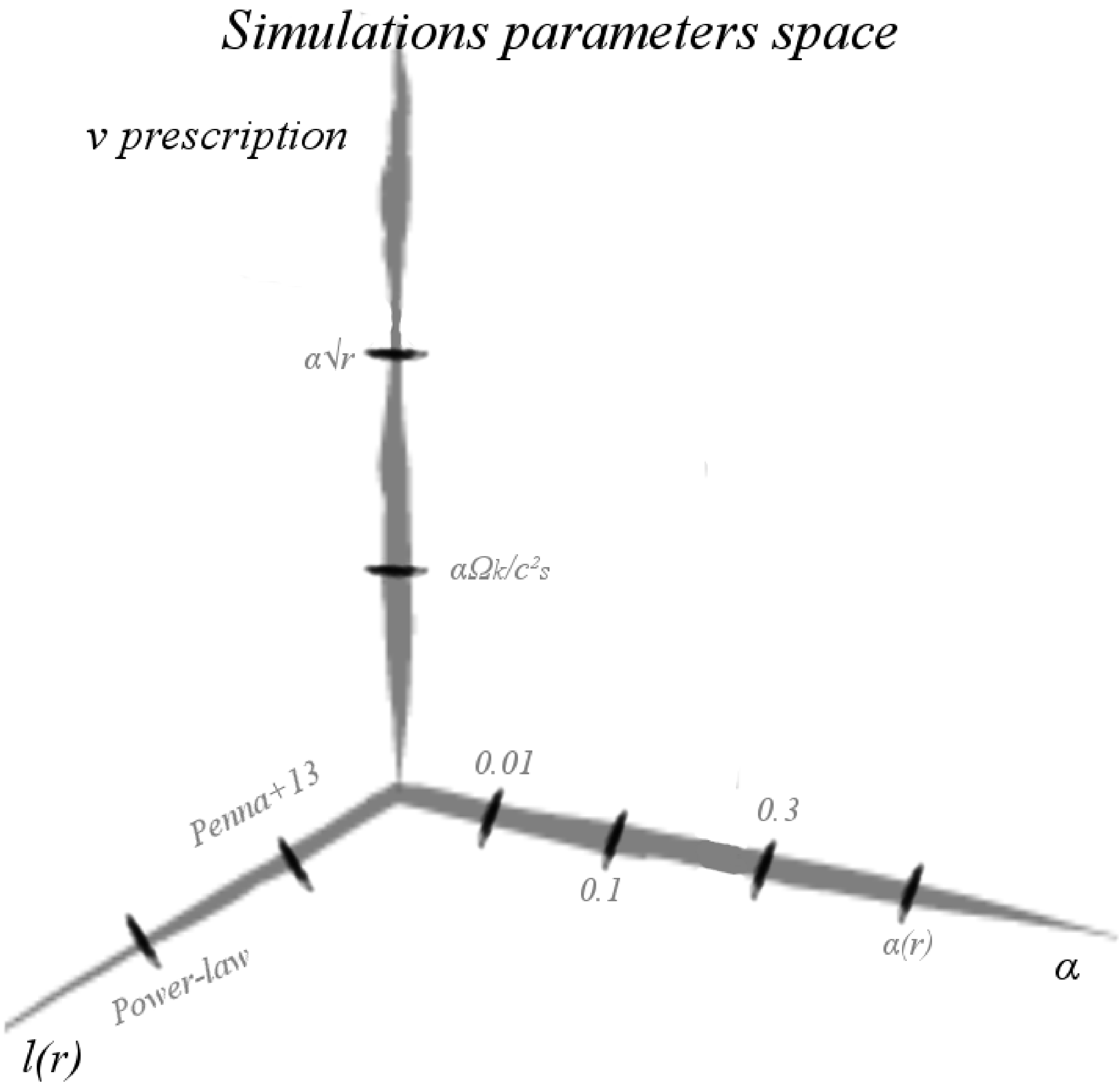

Figure 2.9: Graphic representation of the parameter space covered in our simulations, with the three axis correspond to the model features explored in this work. Please refer to Table 2.1.

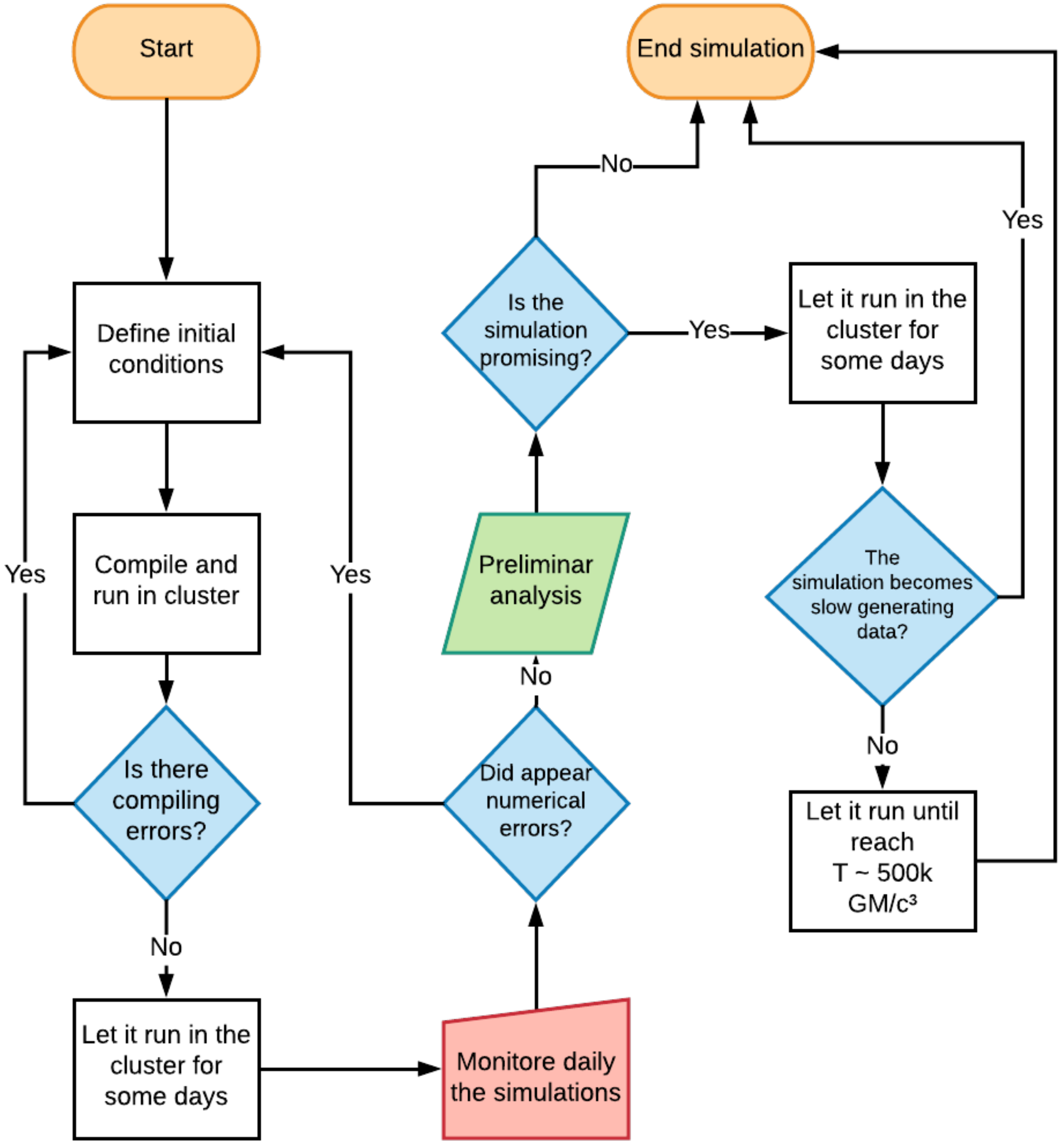

Figure 2.10: The fluxogram of the work in practical terms.

Chapter 3

Results

We now present the results from the analysis of our numerical simulations. In section 3.1 and 3.2, we present in detail the results for three of our models: #ID00, #ID04 and #ID08. In section 3.3 we discuss the other simulations, which had weaker or no winds. Finally, in section 3.4 we present a holistic picture of the results from all our simulations.

3.1 Accretion flow properties

Figure 3.1 shows snapshots of the density maps of models #ID00, #ID04 and #ID08 at different times. Models #ID00 and #ID04 presented a "diffusion-shape"and volume expansion of the torus, but not so dramatic as in model #ID08. The right panel shows stronger ejection than the left and the central ones, with the formation of "diagonal arms"and the torus shape becoming quite disturbed compared to its initial state. #ID08 is one of the simulations the simulation that presented the strongest outflows. In the simulations above, we can see fluid elements being ejected to distances $\gtrsim 500R_S$–which is the initial torus equatorial outer edge adopted. From the velocity field, we can see that there is strong turbulence in the accretion disc, and in the fluid "arms"in the case of #ID08.

Following Stone et al. (1999), we defined the accretion rate as the flux of material through a surface of radius R. We denoted $\dot{M}_{\rm in}$ the mass *inflow* rate and $\dot{M}_{\rm out}$ the mass *outflow* rate, which are defined as

$$\dot{M}_{\rm in}(R) = 4\pi R^2 \int_0^\pi \rho \, \min(v_R, 0) \sin\theta d\theta, \tag{3.1}$$

$$\dot{M}_{\rm out}(R) = 4\pi R^2 \int_0^\pi \rho \, \max(v_R, 0) \sin\theta d\theta. \tag{3.2}$$

The net mass accretion rate is

$$\dot{M}_{\rm acc} = \dot{M}_{\rm in} + \dot{M}_{\rm out}. \tag{3.3}$$

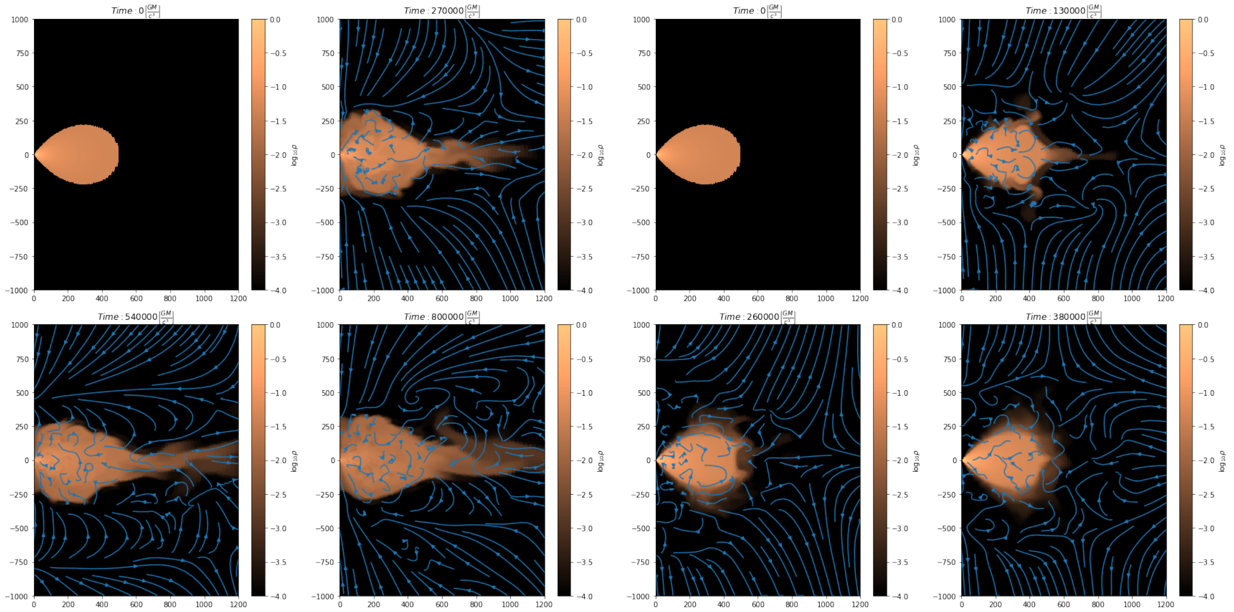

(a) #ID00 (b) #ID04

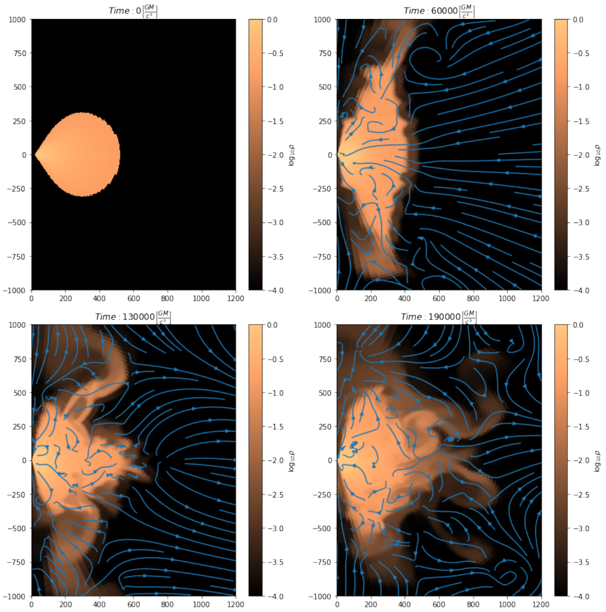

(c) #ID00

Figure 3.1: Snapshots of the density map for simulations #ID00 (left panel), #ID04 (center panel) and #ID08 (right panel), where the color corresponds to $\log \rho(\mathbf{r})$. Here we can see how the torus evolves and changes its shape as time advances; in particular, we can see outflowing material reaching distances further than $500R_S$. Blue arrows correspond to the velocity field, indicating that there is turbulence in the regions with higher densities, located mainly in the torus core.

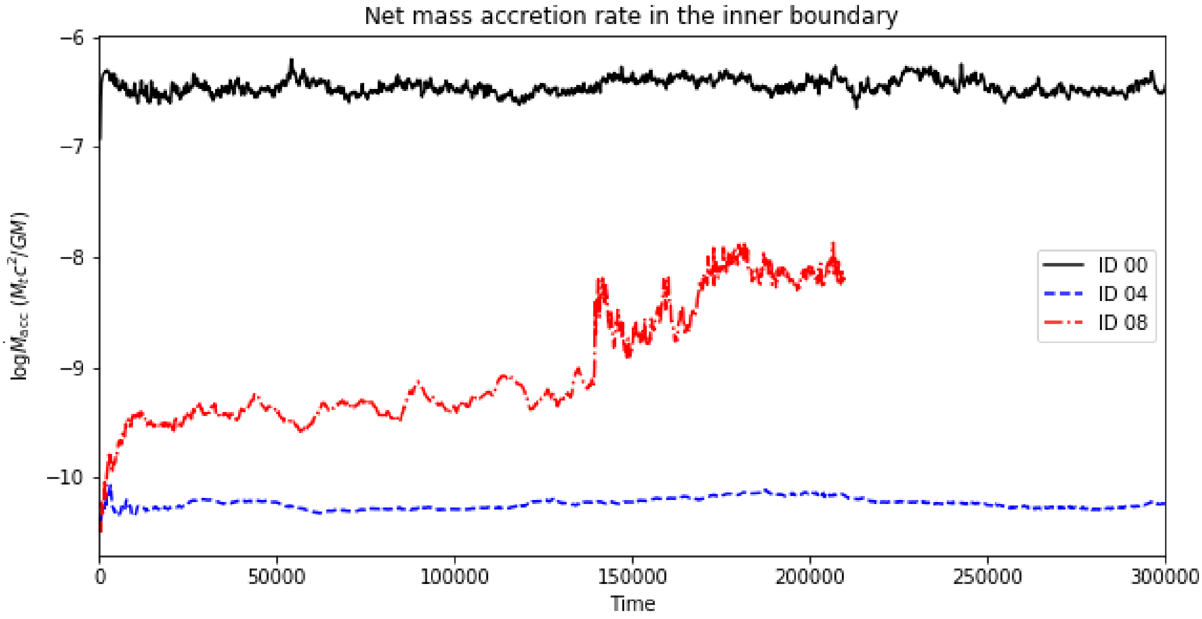

Figure 3.2: Net mass accretion rate in the inner boundary of the simulation, $R \approx 1.5R_S$. Each line represents one of the three simulations, #ID00 is the black solid line, #ID04 is the dashed red line and #ID08 is the dot-dashed blue line.

Figure 3.2 shows the net mass accretion rate calculated at the inner boundary of the simulation–which represents the event horizon[1]. Each line represent one of the previously chosen simulations. In this plot is very clear that the viscosity profile has strong impact in the mass accretion rate; for instance, simulations with the SS-viscosity have much weaker mass accretion rates. The accretion rates for #ID00, #ID04 and #ID08 reach, respectively, a mean value of $10^{-6.5}$, $10^{-(8.-9.)}$ and 10^{-10} in units of M_0c^3/GM where M_0 is the torus initial total mass. In this work we defined $M_0 = \int \rho(\mathbf{r}, t = 0)dV$, with the following normalization: $\max(\rho) = 1$.

In figure 3.3, we show the radial dependence of the mass flow rates computed at the end of each simulation, around the equatorial plane, angle-averaged between $85° - 95°$ and time-averaged in the last $\sim 1000GM/c^3$. The color of the net mass accretion rate curve in Figure 3.3 indicates the dominant mode of mass flux–outflow or inflow. We found noticeable differences between the accretion pattern for the two adopted viscosity prescriptions. For ST we see a constant net mass accretion rate until some oscillations in certain radius. Instead of this constant behaviour, for SS simulations we got a constant net mass accretion rate until $R \sim 30R_S$ and after $\dot{M}_{acc}$ starts to increase until $R \sim 250R_S$,

---

[1] Note that since this is a Newtonian simulation, properly speaking we cannot define a perfectly absorbing event horizon boundary.

which is approximately half of the original size of the disc. The $\dot{M}_{acc}$ is much weaker in SS simulations, but in these simulations if we compare inflow rate and outflow rate we can see that they have very close values for inflow and outflow, since smaller radii ($R \approx 5R_S$), in the ST simulation outflow and inflow become close only at ($R \sim 100R_S$). For SS simulations the increasing behaviour of $\dot{m}_{acc}$ indicates mass accumulation in the central parts of the disc.

The equatorial density profile in the accretion disc, angle-averaged and time-averaged in the same way as the accretion rate in the previous paragraph, is shown in Figure 3.4. As can be seen in the figure, the density is well-approximated by a power-law of the form $\rho \propto r^{-p}$ in the $r = 10 - 400R_S$ range, with the value of the power-law index p in the range $0.48 - 1.33$ as indicated for each model in the panels. The exact value of these slopes are related to the viscosity and the initial $l(r)$ profile, i.e. the initial conditions. The resulting power-law dependence of $\rho(r)$ and the fact that $p < 1.5$ are in agreement with expectations of the ADIOS model (Blandford and Begelman, 1999). It is also in agreement with previous hydrodynamical simulations (Stone et al., 1999; Yuan et al., 2012).

For simulations with a SS viscosity, we saw an increase in the value of max(ρ)–which was initially 1. For instance, the peak density in model ID08 increased from 1 to over 10, indicating an accumulation of mass in the equator of the disk. We saw no evidence for mass accumulation in the model with a ST viscosity, with max(ρ) keeping its value as ≈ 1.

3.1.1 Outflows and the Bernoulli parameter

Traditionally, the Bernoulli parameter Be has been used as an indicator of the presence of unbound gas in numerical simulations (Narayan and Yi, 1994; Narayan et al., 2012; Yuan et al., 2012). Be is defined as

$$Be = \frac{v^2}{2} + \gamma\frac{P}{\rho} + \psi \tag{3.4}$$

and for a stationary, laminar flow, Be can be interpreted as a quantity that measures how much the gas is gravitationally bound to the central mass. $Be < 0$ indicates a bound particle and $Be > 0$ a particle able to escape to infinity.This is the reason why positive values of Be have been taken as indicating the presence of unbound outflows in numerical simulations of BH accretion. On the other hand, the positivity of Be does not guarantee that a gas packet will be ejected, since Be can change its sign in a viscous flow as discussed by (Yuan et al., 2015). In any case, we analyzed the Be-field behaviour in our models.

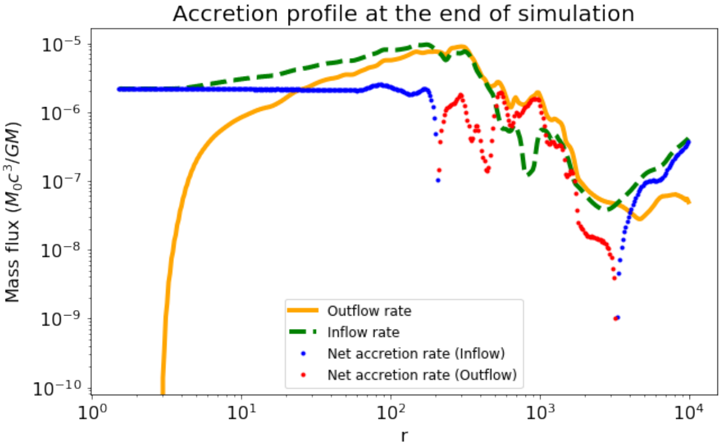

(a) #ID00

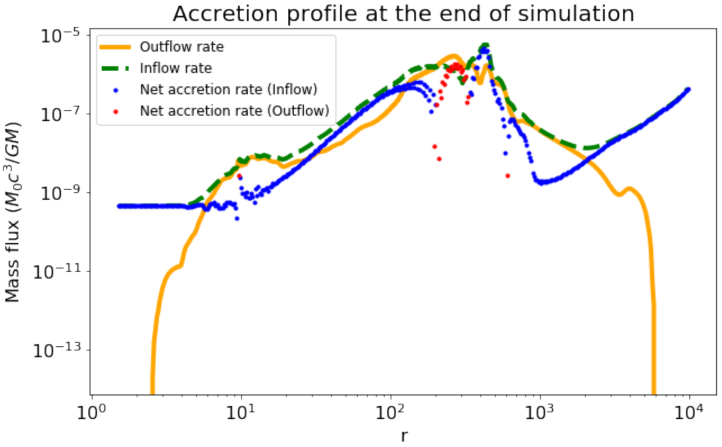

(a) #ID04

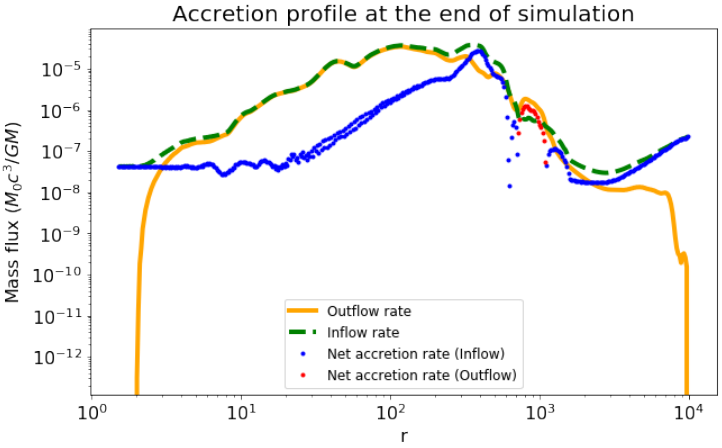

(c) #ID08

Figure 3.3: Mass flux radial profiles for the three main simulations, angle-averaged around the equatorial plane, taken at the final time of each model. The solid orange, dashed green and dotted lines correspond to the inflow rate, outflow rate and net accretion rate, respectively. The color of the dotted line indicates the dominant flow mode: blue if inflow dominates, red if outflow dominates.

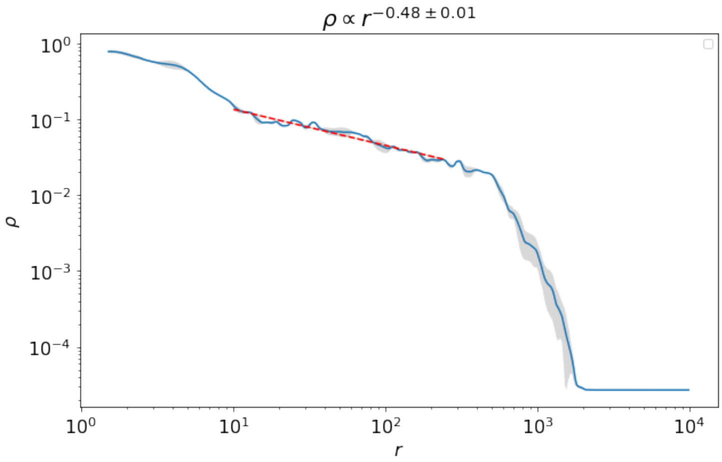

(a) #ID00

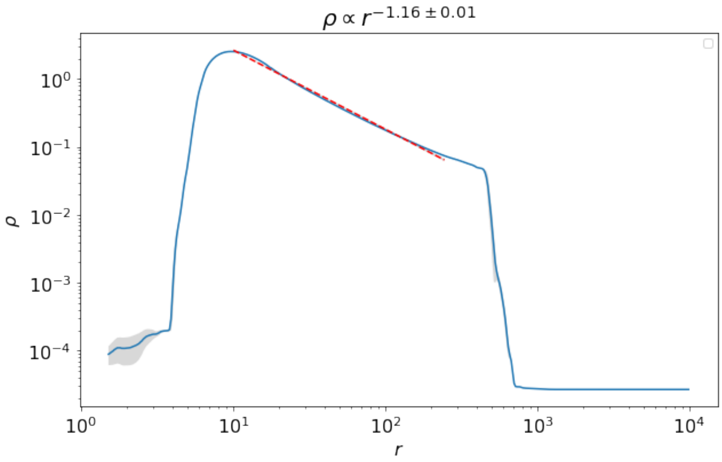

(a) #ID04

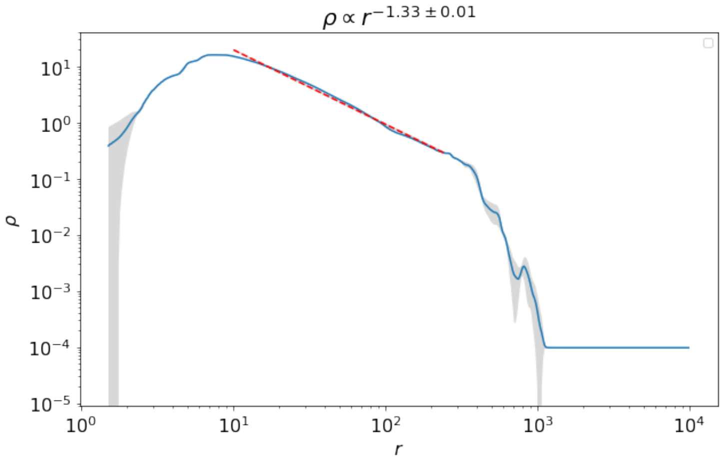

(c) #ID08

Figure 3.4: Density profiles for the three main simulations, $\rho(R)$, around the equatorial plane, it was angle averaged between $85° - 95°$. These profiles were taken in time t explicit in the title of each panel. The solid blue line is the density extracted from the simulation, the unit are in code unit of the defined ρ_0. The dashed red line is the adjust in the "linear region", adopted between $10 - 300R_S$.

In our simulations, Be is positive in most parts of the flow with the exception of the innermost parts located at $R \lesssim 50 R_S$. In order to identify sites of gas ejection, we looked for the regions in the simulation where $Be > 0$ and $V_R > 0$. These regions are red-coloured in Figure 3.5. Throughout the evolution of model 04, we see evidence for a continuous wind with positive Be above and below the accretion disc. There is no such behaviour in model 00. In model 08, we see this outflow at different moments of the run, but puzzling enough it is not present at the end of the simulation. We also see a different kind of outflow occurring at the equatorial region of the disc with $R > R_{\rm out}$ due to the viscous diffusion of matter with excess angular momentum, which moves towards larger radii from the outer edge of the disc. However, in a more realistic environment this region will be dominated by gas inflowing from larger radii; this is not contemplated in our setup that does not consider material injection.

3.1.2 Efficiency of wind production

We now present our results related to the energetics of the winds produced in our simulations. Quantifying the energy outflows from SMBHs is instrumental in the understanding of the coevolution between SMBHs and their host galaxies, since the energy deposited by BH winds can potentially offset gas cooling and quench star formation (cf. introduction). From our simulations, we are able to compute separately the energy outflow rate through winds, $\dot{E}_{\rm wind}$, and the mass accretion rate onto the BH, $\dot{M}$. We then defined a "wind efficiency factor" η as

$$\dot{E}_{\rm wind} = \eta \dot{M} c^2. \tag{3.5}$$

which is the quantity we quote in this paper. Before turning to this efficiency, we need to define what we mean by $\dot{E}_{\rm wind}$ and $\dot{M}$.

Typically, in applications of AGN feedback such as cosmological simulations of galaxy evolution, the authors estimate the feedback power from a mass accretion rate provided to the BH near its Bondi radius $R_{\rm Bondi}$–usually the Bondi accretion rate (e.g. Di Matteo et al. 2005; Sijacki et al. 2015). For consistency with such works, in our simulations we defined $\dot{M}$ in 3.5 as the mass accretion rate at the initial outer radius $R_{\rm out}$ of our accretion flow,

$$\dot{M} \equiv \dot{M}_{\rm in}(R_{\rm out}) \tag{3.6}$$

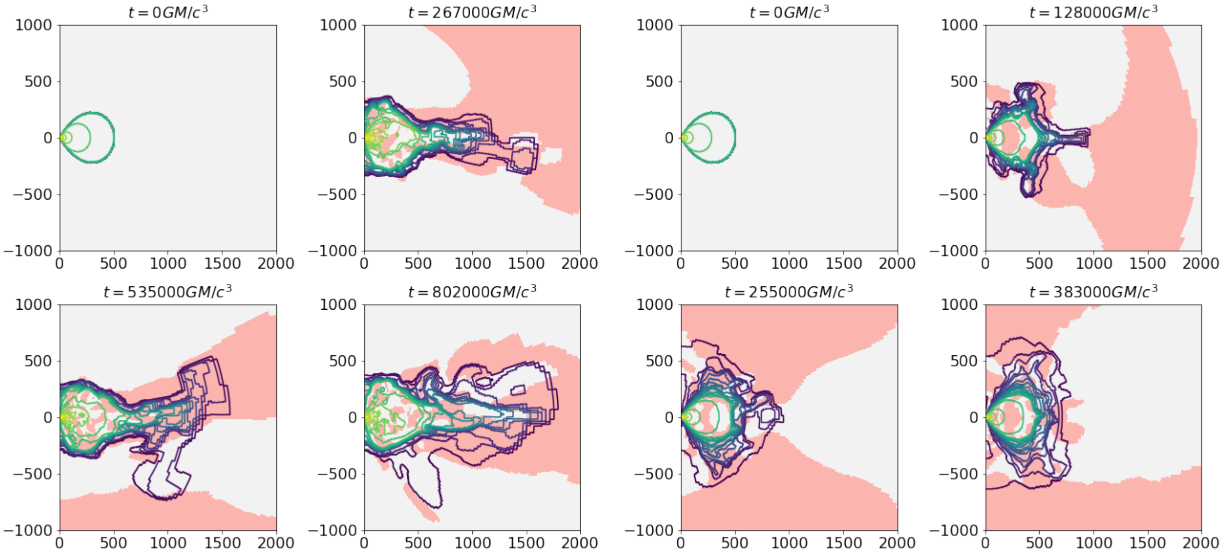

(a) #ID00

(b) #ID04

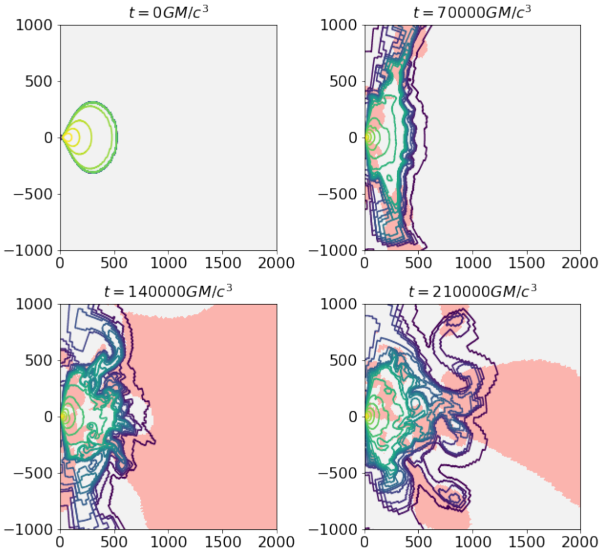

(c) #ID00

Figure 3.5: Outflow regions based on the Bernoulli parameter and radial velocity. Red-shaded areas correspond to potential outflows where $Be > 0$ and $v_R > 0$ where there is a higher chance of gas being ejected and getting unbound. The contours indicate isodensity lines.

which is computed using equation 3.1. We choose to compute $\dot{M}$ at this radius because in our case this is a more appropriate estimate of the outer accretion rate.

The energy outflow rate was calculated as the surface integral

$$\dot{E}_{\rm wind} = \int \epsilon \max(v_R, 0) dA \tag{3.7}$$

calculated at $R = R_{\rm out}$ and only within the angle intervals $15° \leq \theta \leq 45°$ or $135° \leq \theta \leq 165°$ as defined in section 3.2.

With the integral defined in the above equation, when computing the energy rate we will automatically consider only fluid elements with $v_R > 0$. ϵ is the energy density taking into account the kinetic, thermal and gravitational contributions, defined as

$$\epsilon(\mathbf{r}) = \rho(\mathbf{r})\frac{v(\mathbf{r})^2}{2} + \frac{\gamma}{\gamma - 1}p(\mathbf{r}) - \frac{GM}{R - R_S}. \tag{3.8}$$

Therefore, $\dot{E}_{wind}$ is the total power (minus rest mass energy) carried by outflowing gas that crosses the spherical surface at $R = R_{\rm out}$, not taking into account the poles and the accretion disc domain.

Now we are in a position to present the resulting efficiency of wind production. The temporal evolution of η for the three main simulations is presented in Figure 3.6. Each simulation had a strikingly different behavior of $\eta(t)$ with respect to each other. The strongest winds are found in model #ID08–supporting the conclusion from the density maps in Figure 3.1. For instance, at $t \sim 50000 GM/c^3$ the efficiency peaks at $\eta \approx 1$, i.e. the wind power is comparable to the instantaneous accretion power. Afterwards, η drops to a flat value around 10^{-3} in the remaining simulation time.

For models #ID00 and #ID04 there is no continuous outflow. Instead, model #ID00 displays only a timid outflow burst at $t \sim 120000 GM/c^3$ with a peak $\eta \approx 10^{-3}$, lasting for $\Delta t \approx 10000 GM/c^3$. Model #ID04 displayed intermittent periods of gas ejection with peak efficiencies ranging between 10^{-2} and 10^{-3}. Despite η's variability in all models, we did not find any evidence of periodical oscillations.

3.2 Analysis using tracer particles

One of the strengths of using the technique of tracer particles (section 2.5) is that we are able to quantify more precisely the amount of mass lost from the disc due to outflows by tracking the amount of mass carried by each particle. Using the tracer particles method,

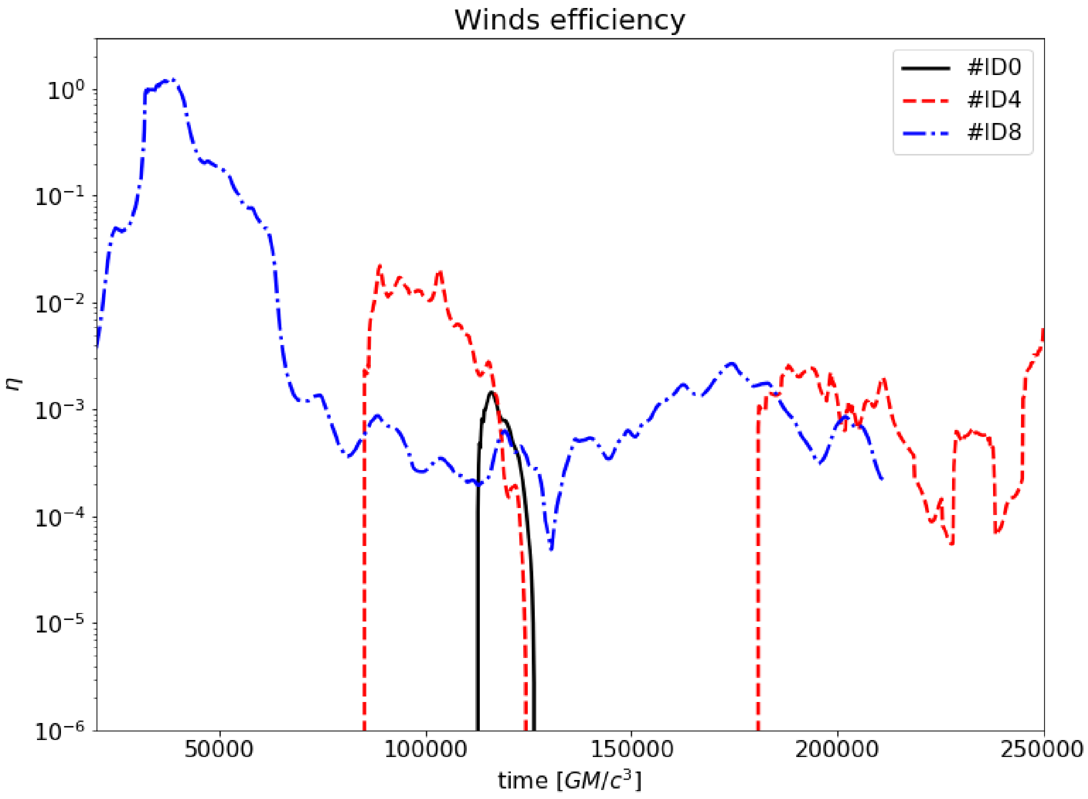

Figure 3.6: Temporal evolution of the wind efficiency η as defined in equation 3.5 for the simulations #ID00 (solid black line), #ID04 (dashed red line) and #ID08 (dot-dashed blue line).

we define the fraction of ejected particles–i.e. a measure of the relative fraction of gas lost from the disc due to outflows–considering the simple and real outflow criteria respectively as

$$f_{\mathrm{ej;simple}} = \frac{n(R_{\mathrm{final}} > R(t = t_0;\ \mathrm{wind})}{n_{\mathrm{total}}(\mathrm{disc})}, \tag{3.9}$$

$$f_{\mathrm{ej;real}} = \frac{n(R_{\mathrm{final}} > R_{\mathrm{out}};\ \mathrm{wind})}{n_{\mathrm{total}}(\mathrm{disc})}, \tag{3.10}$$

where $n(R_{\mathrm{final}} > R(t = t_0;\ \mathrm{wind})$ is the number of particles that respect the necessary conditions to be considered outflowing particles, n_{total} is the initial number of particles released from the disc. For each value of launching radius $R(t = t_0)$–the radius at which we initially place particles uniformly distributed in θ–we launch 50 particles and compute these fractions, displaying the results in Figure 3.7.

Comparing the three simulations in Fig. 3.7, according to the "simple outflow" criterion model #ID08 is clearly is the simulation with higher fraction of particles ejected–$\sim$ 25%– of all initial particles, while models #ID00 and #ID04 presented respectively $\sim$ 5% and $\sim$ 12%. Using the "real outflow" criterion–which is a more stringent criterion for mass-loss–the fractions for models #ID00, #ID04 and #ID08 are respectively $\sim$ 5%, $\sim$ 7% and $\sim$ 9%. We found that the three simulations ejected a similar number of particles.

In Figure 3.8 we show the mass and energy carried away by the outflowing particles in the case of the "real outflow" criterion. We defined the relative fraction of ejected mass f_{mej} and the fraction of ejected energy f_{enej} as

$$\begin{aligned} f_{\mathrm{mej}} &= \frac{\text{mass in tracer particles lost in outflows}}{\text{total mass of tracer particles}} \\ &= \frac{\sum_k m_k \Theta[R_k(t = t_{\mathrm{final}}) - R_{\mathrm{out}}]}{\sum_k m_k}, \end{aligned} \tag{3.11}$$

where the sums are carried over all tracer particles and Θ is the Heaviside function. We assumed that a particle k does not lose mass as it moves, such that the mass of each particle is constant over time and given by

$$m_k(t) = \mathrm{const} = m_k(t_0) = \rho[\mathbf{r}_k(t_0)]\delta V, \tag{3.12}$$

where we assume that all particles occupy the same small volume $\delta V = \mathrm{const}$. The specific value that we adopt for δV does not matter because when computing f_{mej} using equation

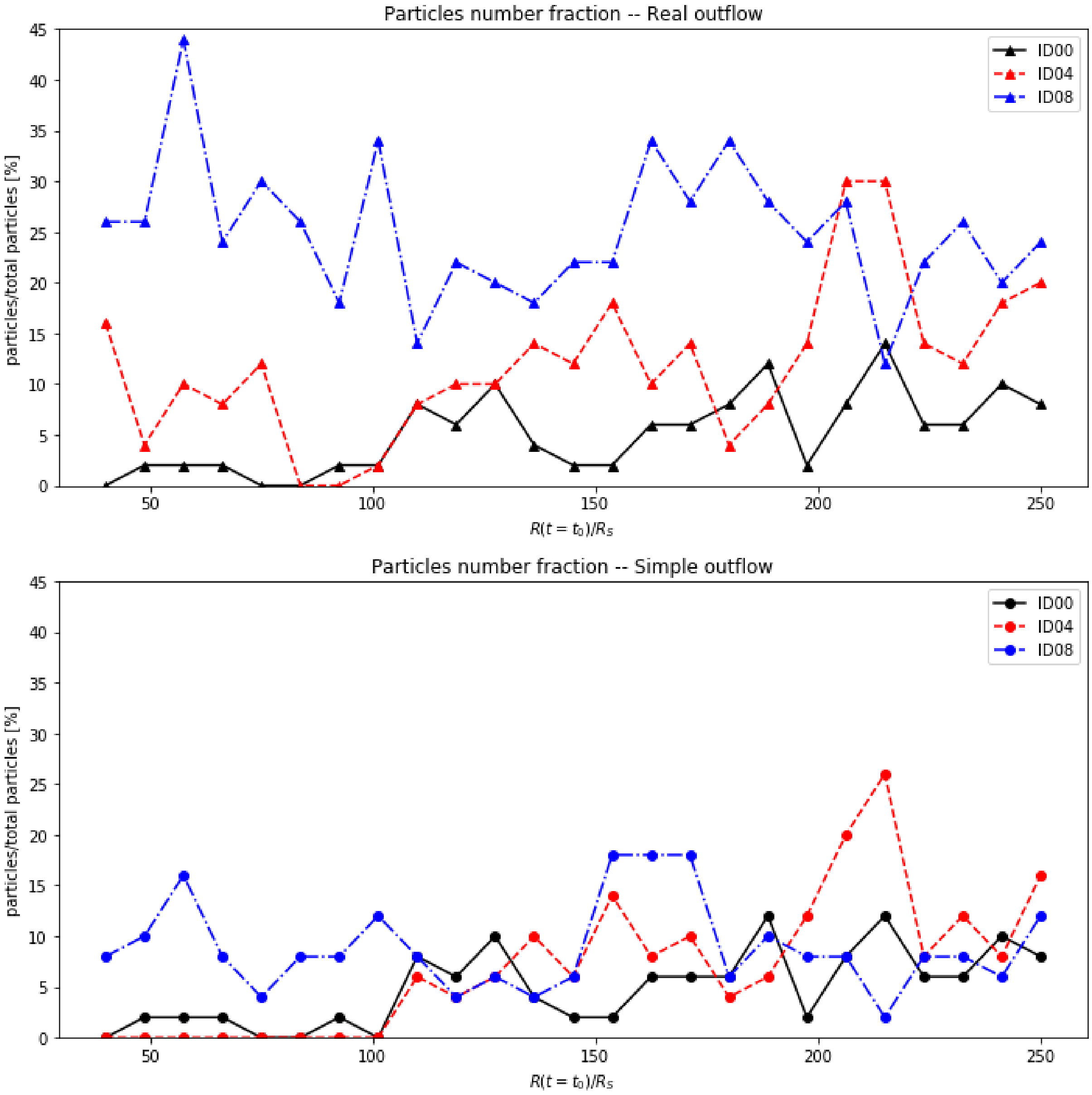
Particles number fraction -- Real outflow

Particles number fraction -- Simple outflow

Figure 3.7: Fraction of particles lost in outflows according to the tracer particles method. The top panel is for the real outflow and the bottom for the simple outflow as defined in the text. Models #ID00, #ID04 and #ID08 correspond respectively to the solid black line, the dashed red line and the dot-dashed blue line.

3.11, δV cancels out. Similarly, we defined the relative fraction of ejected energy f_{enej} as

$$f_{\mathrm{enej}} = \frac{\sum_k E_k(t = t_{\mathrm{final}})\Theta[R_k(t = t_{\mathrm{final}}) - R_{\mathrm{out}}]}{\sum_k E_k(t = t_0)} \tag{3.13}$$

where the energy is defined as $E(\mathbf{r}) = \epsilon(\mathbf{r})\delta V$ and ϵ is the energy density from (3.8).

From these two plots we can see that the ejected energy follows the same pattern as the mass ejection. In addition, at all radii, the amounts of mass (or energy) lost are similar, with the exception of the innermost parts of the flow for model #ID08. In the bottom panel, there is a clearly a patter of decreasing average energy per ejected particle as the radius increases. For $R \gtrsim 50 R_S$, $\overline{E}_p(R)$ can be approximated by a function of the form.

$$\overline{E}_p(R) \propto 10^{-\frac{R}{R_*}}. \tag{3.14}$$

For our simulations the results of R_* for all simulations were showed in table 3.1. These radii can be interpreted as the characteristic limit radii for wind production, with the region $R < R_*$ from which most of the energetic outflows come from. Particles coming from this region are the main candidates to reach distances beyond the gravitational domain of the SMBH.

Mass-loss through winds is not uniformly distributed across all radii. In order to quantify how far a particle originated in a certain radius can go, we plotted the quantity $R(t_{\mathrm{final}})/R(t_0)$–which we will refer to as wind depth henceforth –in Figure 3.9. Larger values of the wind depth in a given region of the flow indicate that it can produce outflows that reach large distances. As such, Figure 3.9 is tracking the accretion flow regions where the ejected particles come from. The three panels were labeled for each simulation and we considered only particles that are in the wind region. In models 04 and 08 we see bipolar outflows, whereas model 00 displays a strange asymmetry–an unipolar outflow–with all the ejections occurring in the same side, which is very unique when compared with the other simulations we performed. In models 00 and 04, the ejection occurred mainly in the torus corona–similarly to coronally-driven winds–whereas model 08 seems to produce winds from all regions of the disc with a more homogeneous ejection region, with outflows coming even from the equator.

An important parameter to be analyzed in these simulations are the velocity of these ejected particles, the distribution of their velocities, for each main simulation, are in the panels of figure 3.10. In the figure we divided the sample in two types of particles, the ones

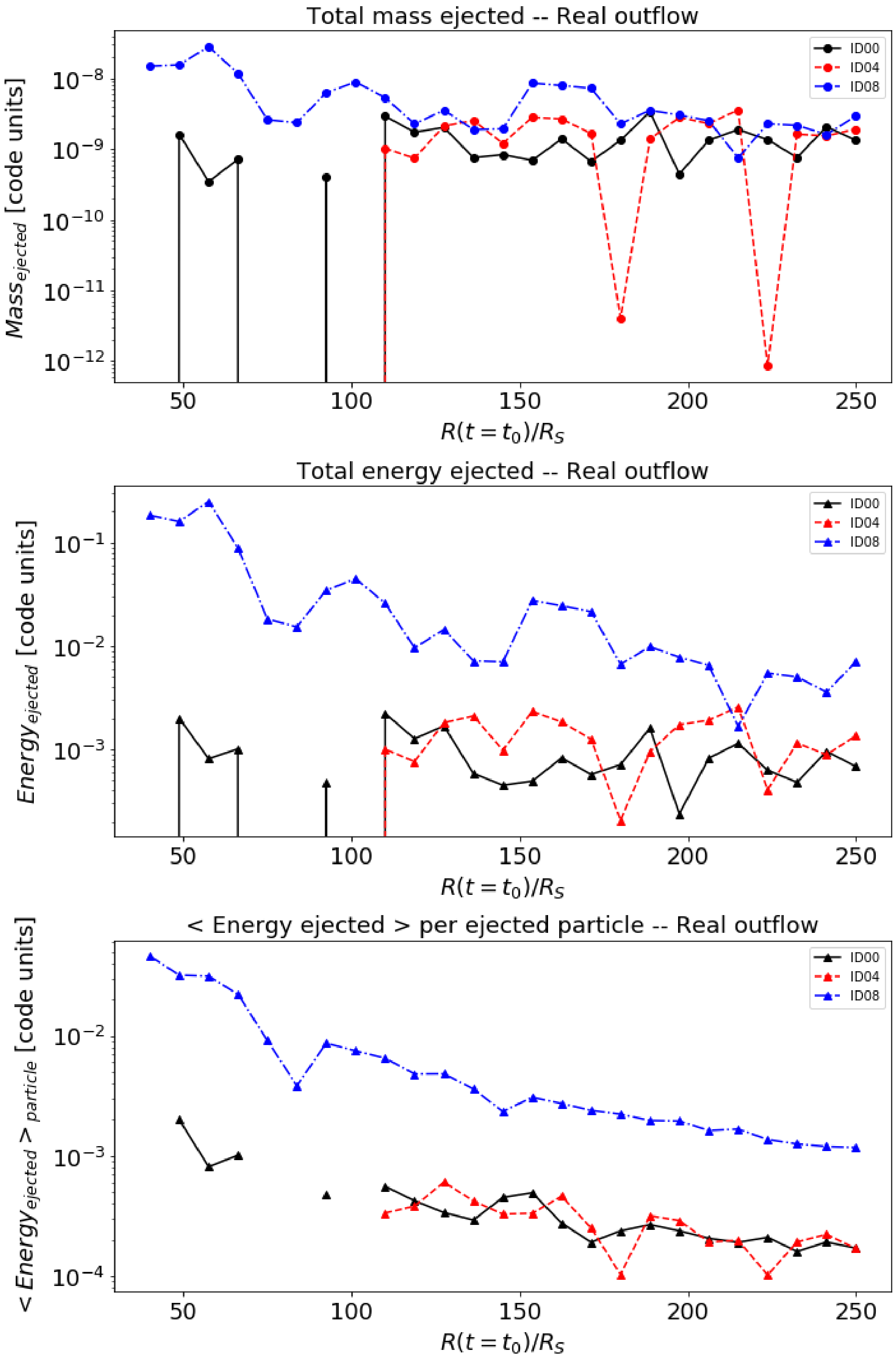

Figure 3.8: Top and middle panels: total ejected mass and energy in the three simulations in code units. Models #ID00, #ID04 and #ID08 are displayed as solid black line, dashed red line and dot-dashed blue line, respectively. Here we plotted the square root of these quantities, but only for scale reasons. We can see that the loss of both mass and energy is more pronounced in model #ID08 compared to the other two–i.e. the resulting outflows in this model are stronger. Bottom panel: mean energy carried by each particle ejected from $R(t = t_0)$.

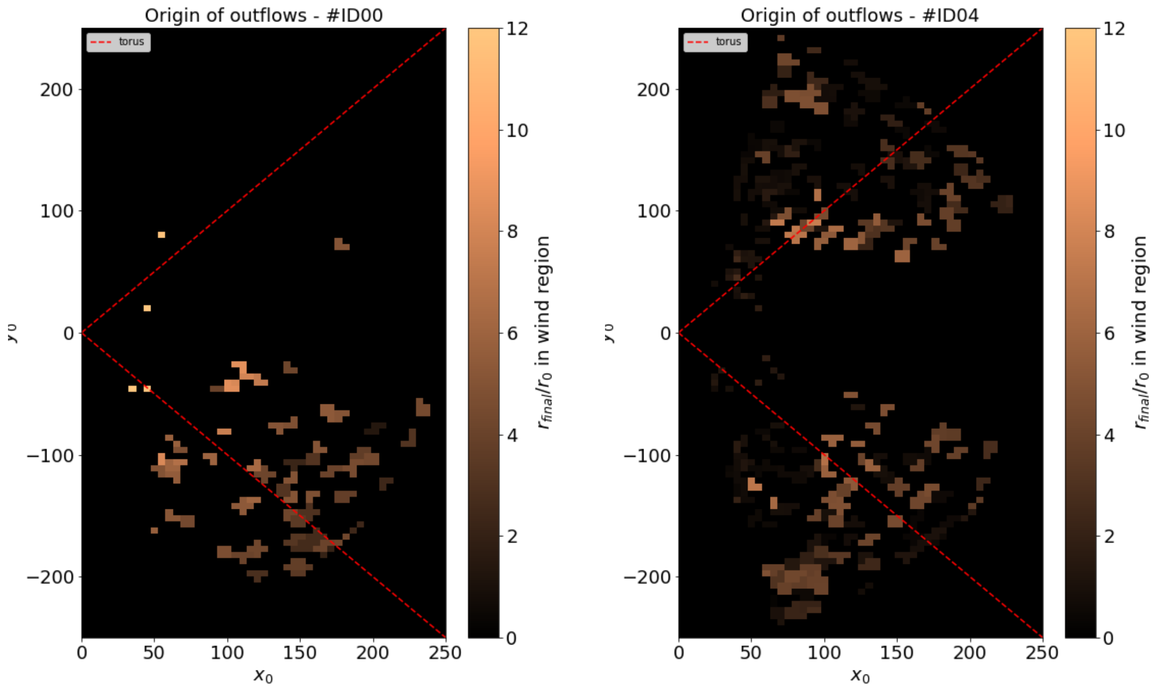

(a) #ID00 (b) #ID04

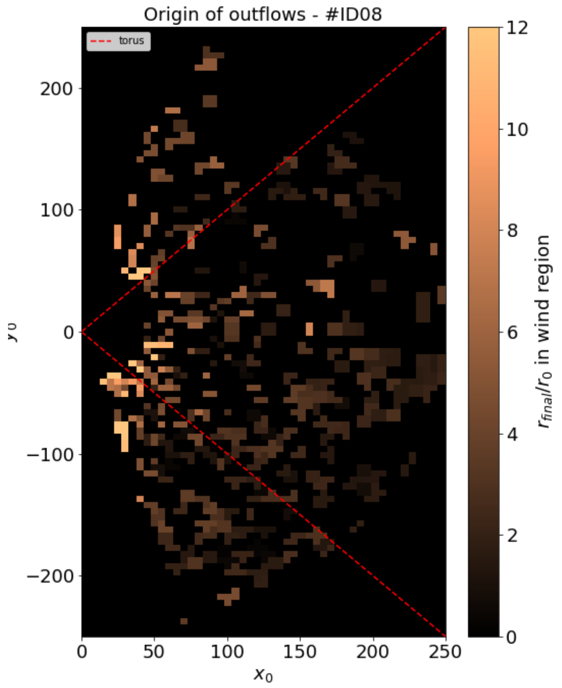

(c) #ID08

Figure 3.9: Map of the ejection fraction, for a particle in the position (R, θ) in t_0. This map shows the range of the particle ejected in that position. The regions with light color are the areas where particles are ejected more efficiently, in other words, these are the regions that produce the winds in the simulations.

with $v_R > 0$ (blue) and the other ones with $v_R < 0$ (grey). For outflows is straightforward to think in particles with velocity pointed in direction of the exterior of the analyzed system, but we find that are some particles with negative velocities, that can maybe come back to the accretion disc. #ID00 had a low rate of outflow and the few ejected particles had in average negative radial velocities, they potentially can come back to the disc, especially the ones with higher velocities ($v_R \gtrsim 10^{-3}c$). #ID04 and #ID08 had ejected particles with negative velocities, but the sample are dominated by ejected particles with positive radial velocity, that still can reach higher distances and characterize a true outflow.

Considering only the case with $v_R > 0$, the median velocities for outflow particles was showed in table 3.1, , for all simulations $\overline{v}_{\mathrm{out}}$ was in the range 0.001-0.006c.. The ejected particles presented non-relativistic velocities, the maximum velocity, even in #ID08, did not surpass $0.05c$.

3.3 Other simulations

Besides these three simulation discussed in previous sections, there was other simulations, which we chose to not expose in same details. Following the table 2.1, we briefly described the remaining simulations in the next subsections. In figures 3.11 and 3.12 there are the density maps in the last snapshot of each simulation.

3.3.1 #ID01

The unique difference between #ID00 and #ID01 is the adopted value of α, in this simulation $\alpha = 0.1$, which turns the effects of viscosity more pronounced. In this configuration, the disc loses its original form around $t = 60000 \left[\frac{GM}{c^3}\right]$ and there is no clear outflows in the wind region, following our previous definitions. Simulation #ID01 becomes very similar to the shape of #ID00 showed in the left panel of figure 3.4 but in small time and with a 10 times higher accretion rate.

The values for the equatorial density profile power-law are shown in 3.1. The profile indicates the second lowest value of p, following the ADAF model, this should indicate the presence of mass loss via outflows, but the outflow was not detected, like #ID00. This simulation presented a η function similar to #ID00 and the fraction of ejected energy calculated via particles in the system was $\sim 2\%$, a bit below that the obtained value from

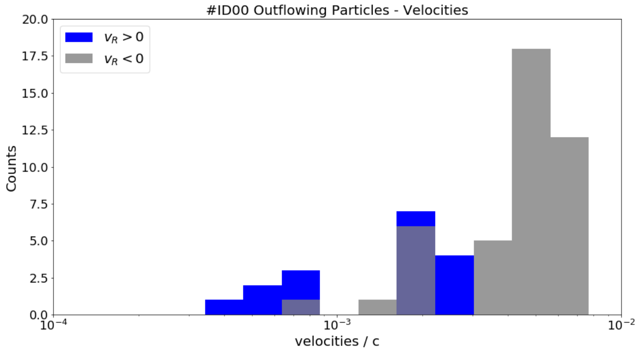

(a) #ID00

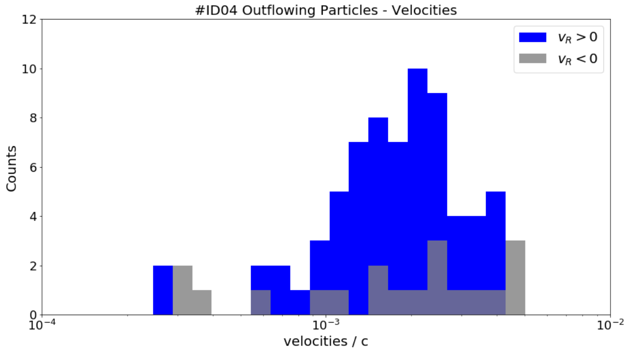

(b) #ID04

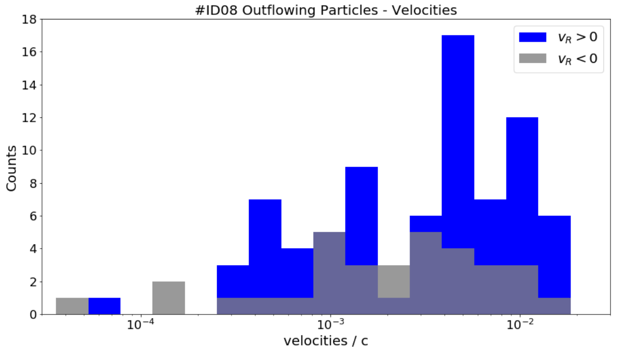

(c) #ID08

Figure 3.10: Each panel corresponds to the distribution of velocities of the ejected particles for the labeled simulation. These histograms displays the averaged velocity of the ejected particles in the last $\sim 1000GM/c^3$ of each simulation. The blue columns represented the population of particles with $v_R > 0$, the grey columns represented the population of particles with $v_R < 0$.

#ID00.

3.3.2 #ID02

This simulation is very close to #ID04, they share the same specific angular momentum profile and viscosity prescription (SS), the main α value of both are very close, it is not a surprise that the results are very similar too. We can see that these two simulations share the same value of p for the equatorial density profile $\rho(r) \propto r^p$ in table 3.1, η function shape, the ejection rates and launching region of this simulation are, besides small variations, essentially the same as #ID04. The effects of the variation of $\alpha(R)$ in the innermost part of the simulation does not change the dynamics of ejection in the wind region and in the outer parts of the accretion disc.

3.3.3 #ID03

#ID03 is very similar to both #ID02 and #ID04 in the original setup, the only difference is in the choice of α. In this simulation $\alpha = 0.3$ which means a higher viscosity effect, but there was no much difference between this simulation and the other two, the only difference is that #ID03 have a slightly small fraction of ejected energy than its similar simulations, with: $f_{\rm ej}^{02} = 2.75\%$, $f_{\rm ej}^{03} = 1.25\%$ and $f_{\rm ej}^{04} = 2.15\%$. All member of this trio had essentially the same time of simulation $\sim 400000 GM/c^3$, and presented very similar results in our main parameters (accretion rate, η, fraction of ejected energy, etc).

3.3.4 #ID05

This simulation was performed with a constant specific angular moment, $l(r) = \text{const}$ and a ST-type viscosity profile. It presented a evolution marked by a very strong inflow in the first $10000 GM/c^3$, with the material essentially free-falling onto the BH. During the infall, the material piled-up in the inner parts of the disc and formed a spherical accretion flow. We found a jet-like structure arisen in the simulation which has an hydrodynamic origin for the following reason. Material was accreted quite fast due to the strong α-viscosity. The disc overfeeds the BH, giving it more than it can take and the accretion becomes spherical. Material piles-up along the polar axis, and the ensuing overpressure creates a vertical structure that looks like a jet. All this process occurred considerably fast, within $50000 GM/c^3$ after the beginning of the simulation.

The net mass accretion rate in this simulation is essentially the same as #ID01, but here the rotation did not sustained the disc. It was happened essentially only inflow in this simulation, the number fraction of ejected particles is null, not a single particle escaped to the wind region. The η had two bursts along the simulation time with peak of ~ 0.05, but most of the time $\dot{E}_{wind} = 0$.

3.3.5 #ID06

#ID06 shares the same $l(r)$ with #ID05, but with SS-viscosity profile. This simulation are not similar with any other one. The shape of the disc did not present great changes along the simulation, it maintained its original shape during all the $200000 GM/c^3$. The net mass accretion rate here is a bit higher than the net mass accretion rate observed for #ID02-04 and the density profile is similar to the $\rho(r)$ for #ID05, as it had shown in table 3.1.

The particles for this simulation presented a behaviour similar to the particles of #ID00, the particles have been launched, some were accreted and other followed the external contour of the disc and get ejected in our defined disc region near to $\theta = 90°$, hence we did not consider this ejection as a wind. The the number fraction of ejected particles in wind region was null. But differently from the other simulations with low value of fraction of ejected energy, the η here indicates presence of winds similar to #ID08, which is not consistent with the particle analysis. This come from the diffusion of the huge disc (see panel (a) of figure 2.6), probably the disc diffused and make the calculation of $\dot{E}_{wind}$ unreliable in $R = 500 R_S$, if we calculate the same integral in a further radius like $R = 750 R_S$ we noted that $\dot{E}_{wind} \sim 0$, different of #ID08 which had the same η value for both two radii, $500 R_S$ and $750 R_S$.

3.3.6 #ID07

#ID07 was the simulation with more intense outflows, the fraction of ejected energy is $\sim 20\%$, which is twice the value found for #ID08 in the previous detailed analysis, with a bit smaller time of execution than #ID08. The general aspects of #ID07 were pretty similar to #ID08, they both shared the same specific angular momentum profile and viscosity prescription, the only difference is the α value, $\alpha^{07} = 0.1$ and $\alpha^{08} = 0.3$. There were minor differences in the density maps between the two simulations, #ID07 showed less ejection in the equatorial plane than #ID08, which was observable in the difference in the slope of density profile from table 3.1. The accretion rate and the η of these two simulations are very alike.

The main differences between #ID07 and #ID08 are: (i) the net mass accretion rate plot, for #ID08, bottom panel in figure 3.2, the net mass accretion rate increased with larger radius, the same is observed for #ID07, with close values, but for #ID07 the net mass accretion rate was in the direction of the outflow, while in #ID08 was pointing with the inflow. #ID07 is the only simulation in that the mass outflow rate is more intense than mass inflow rate for $30 \lesssim R \lesssim 300R_S$. And (ii) the velocity distribution of the particles, #ID08 velocity histogram, which is showed in the third panel of figure 3.10, was dominated by particles with $v_R > 0$, for #ID07 there were more particles with $v_R < 0$, near to the half of the total number. The average velocity of the particles in #ID07 were smaller than #ID08, but is still the second highest average velocity of particles from our simulations.

The ejection map of this simulation is very close to the third panel in figure 3.9, both simulations ejected particles from all parts of the disc. #ID07 and #ID08 were similar between each other and very different from the rest of the sample.

3.3.7 #ID09

This simulation had the same specific angular momentum profile as #ID07 and #ID08, but with a different viscosity prescription, which led to a complete different result, there was no outflows. The particles had been mostly accreted and the accretion rate was high, the ejected particles were ejected in the jet region. Similar to #ID05, in this simulation we had a spherical accretion and the emergence of a jet-like structure formed due to the intense loss of angular momentum of the disc, even with the small running time of $\sim 38000GM/c^3$. There was no winds.

The density profile slope was very close to the one found in #ID04 (see table 3.1) but they had completely different accretion modes, the torus format evolution have no similarities between these simulations. The ejection fraction and wind efficiency were both null.

3.3.8 #ID10

#ID10 was the only simulation with the initial condition $l(r) \propto r^{0.4}$ that did not presented numerical errors in the very first steps of the evolution, the implementation of the SS viscosity prescription unfortunately was not possible with this angular momentum profile. The results of this simulation were different from all previous setups.

The accretion disc of this simulation was utterly destroyed in $\sim 120000 \left[\frac{GM}{c^3}\right]$ and left some filaments, that looked like a gaseous wig that keep being accreted. The accretion rate decreased after the destruction of the disc, but even with lowered rate it is still orders of magnitude higher than the accretion rate of the simulations with SS-viscosity (in units of $M_0 c^3/GM$). #ID10 had the highest net mass accretion rate, $\dot{m} =\sim 10^{-4} M_0 \frac{c^3}{GM}$, of all simulations.

The fraction of ejected energy from #ID10 is really close to the value of #ID03, $\sim 1\%$, but its wind efficiency η in the second half of the simulation time is comparable to the value found in #ID08. probably after the torus destruction outflows were produced in the simulation #ID10, but these scenario is not very physical, because we expect a well-behaved accretion disc that could survive for a long time and not a destroyed disc reduced to some gas filaments. Another remarkable feature of this simulation is the value of $p = 1.53$, which is poorly consistent with the assumption of $p < 1.5$, considering that we had small uncertainties in the calculus.

3.4 Overview of results for all models

After the solo analysis of each simulation we proceeded to analyze these results as a whole. In Figure 3.13 we plotted $f_{\rm mej}$ as a function of $\dot{m}(1.25 R_S)$, i.e. it relates our the fraction of mass (or energy since) lost in the wind (cf. equations 3.11 and 3.13) and the net mass accretion rate at the event horizon (more rigorously, at the inner boundary of the simulation). $\dot{m}$ is normalized by the torus initial mass assuming that all simulations had the same total torus mass in the beginning.

Each simulation occupies a different region of the diagram in Figure 3.13. The different viscosity parameterizations adopted are clearly distinguishable, for instance simulations with the ST prescription generated $\dot{m}$ values orders of magnitude higher than the SS profile. Motivated by this considerable difference, we plotted the black dotted line in the

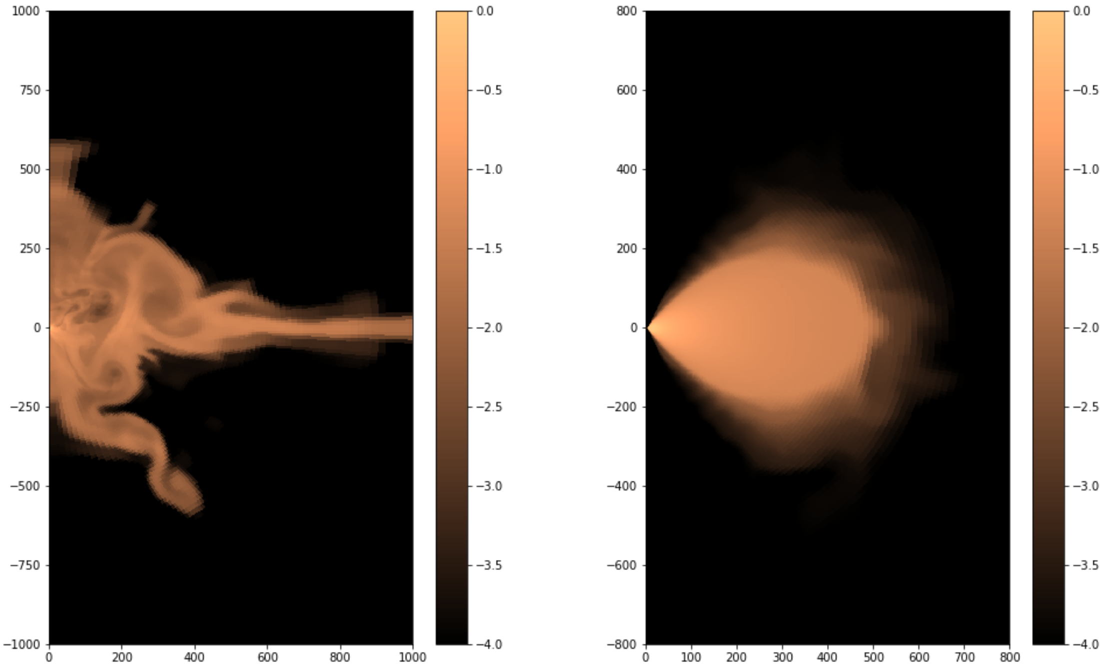

(a) #ID01 (b) #ID02

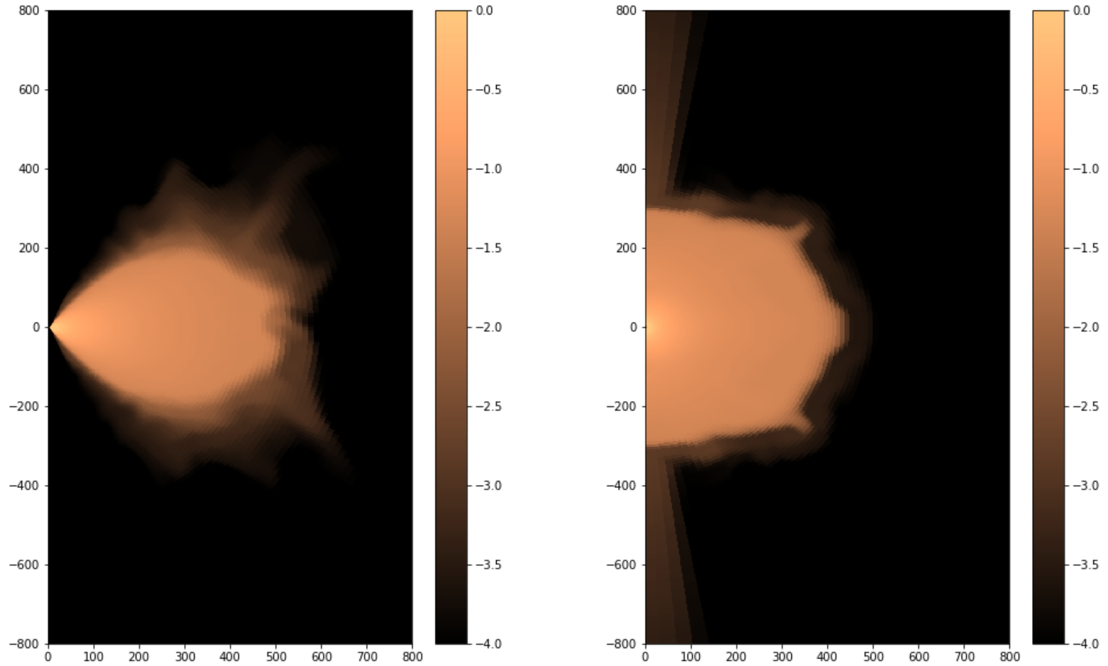

(c) #ID03 (d) #ID05

Figure 3.11: Map density of the simulations in the final moment of each one (2.1).

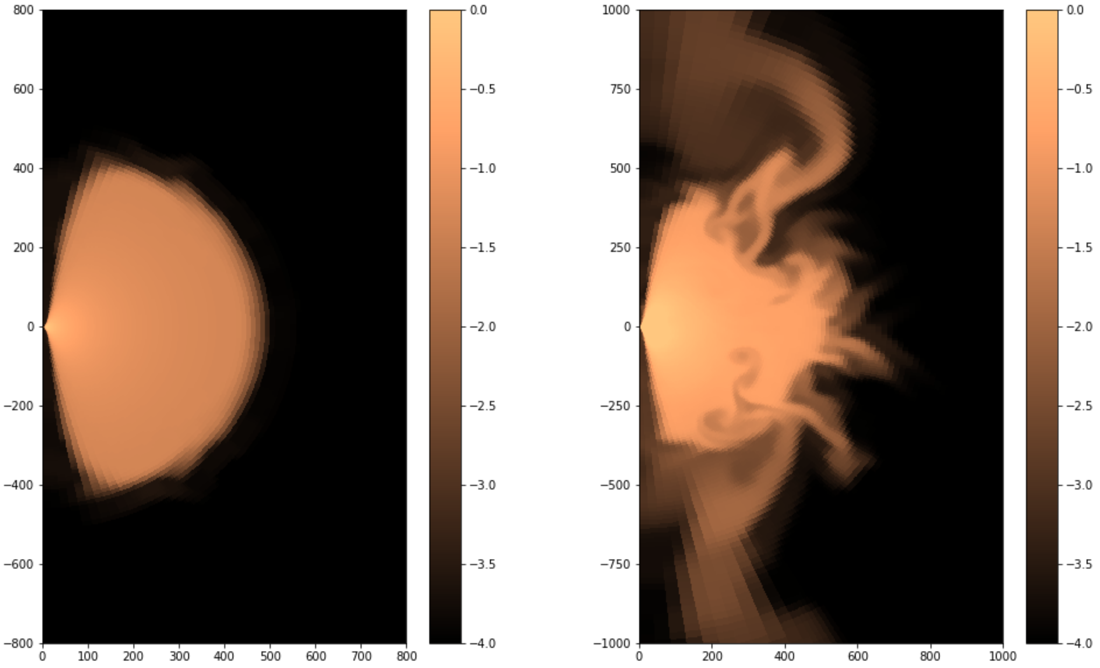

(a) #ID06

(b) #ID07

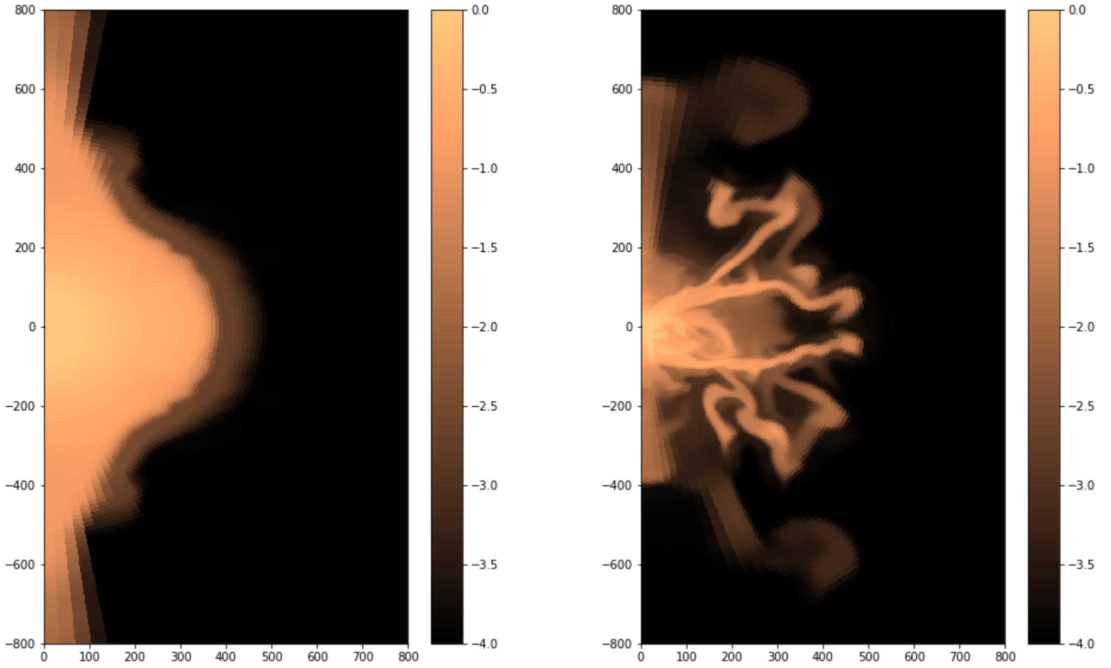

5

(c) #ID09

(d) #ID10

Figure 3.12: Map density of the simulations in the final moment of each one (2.1).

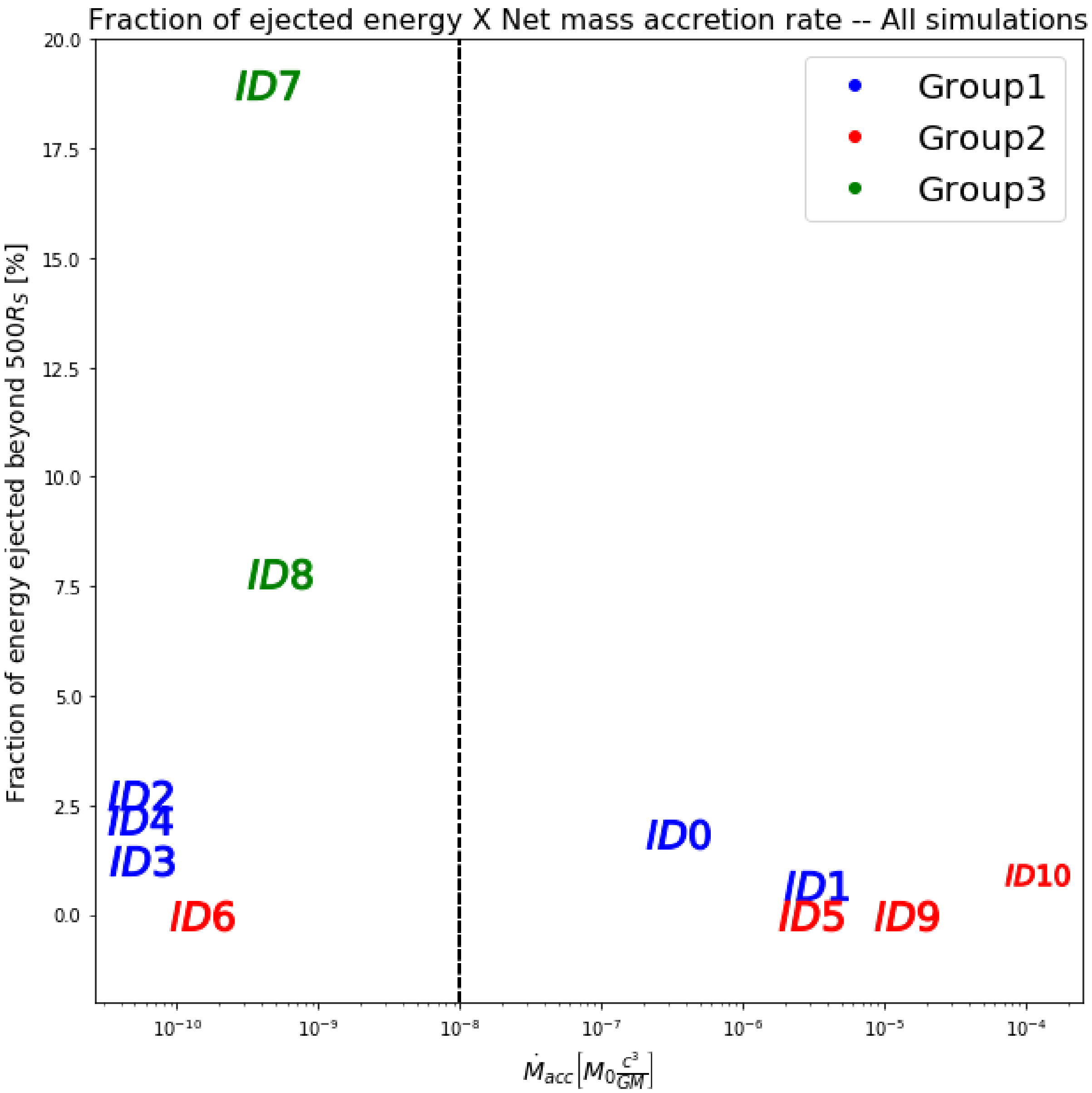

Figure 3.13: Net mass accretion rate $\dot{m}$ versus the fraction of ejected mass (or energy) of the simulations. The labels identify the simulations. We divided them in three groups for the analysis as described in the text. The black dotted line in the center are separating the two regime of viscosity adopted, in the left-side there is the simulations with SS-viscosity, in the right side the ones with ST-viscosity (see section 2.1).

figure to separates these two types of simulations. We divided them in three groups for the analysis:

- Group 1: simulations with the specific angular momentum adapted from Penna et al. (2013)
- Group 2: simulations with power-law $l(r)$ and smallest fraction of ejected energy
- Group 3: simulations with power-law $l(r)$ and highest fraction of ejected energy.

They have some major characteristics considering both fluid and particle analysis:

- **Group 1** had on average 2% of energy ejection, this value seems that does not change drastically with the free parameters of the simulation or the adopted viscosity. The wind flux (see equations (3.7)-(3.5) and figure 3.6) of these simulations was non-continuous, winds were not generated all the time here. The average velocity of the ejected particles here are smaller than the group averaged velocity for Group 3, $\overline{v}_{\rm out}^{\rm G1} \lesssim \overline{v}_{\rm out}^{\rm G3}$

- **Group 2** had the smallest fraction of energy ejected. These simulations presented strong inflow component, except for #ID06, the inflow was so intense in these three that suppressed any outflow. #ID06 did not present the same inflow component as the other ones, but the particles remained inside the big torus all the way (see first panel from figure 2.6). The wind generation pattern of these simulations varied for all simulations. This group presented completely heterogeneous properties.

- **Group 3** are the simulations with the most energetic winds and particles. Models #ID07 and #ID08 are very similar simulations with the only difference in the value of α, as discussed before. The setup consisting of $a = 0.2$ and SS-viscosity presented powerful outflows, with a continuous generation of winds, the highest average velocities from our sample as it was showed in table 3.1.

It is worthwhile asking: considering holistically all the models which produced winds, what is the location in the disc from which the outflowing particles come from, on average? For this purpose, we apply the tracer particles formalism to locate the launching region in the eleven simulations. For each model, we considered only the particle ejected in the wind region–similarly to Figure 3.9–by defining the binary variable

$$\mathrm{ej} = \begin{cases} 1, & \text{if } (\mathbf{r}_{\mathrm{final}} \text{ is in wind region) and } (R_{\mathrm{final}} > R(t_0)) \\ 0, & \text{otherwise.} \end{cases} \tag{3.15}$$

The variable ej informs whether a particle at a given position has been ejected (ej = 1) or not (ej = 0). After creating maps of ej for all simulations, we added them up and computed the average, $\overline{\mathrm{ej}}$. The result can be seen in figure 3.14, where the color scale indicates the likelihood that a particle located at the given position at the beginning of all simulations becomes part of an outflow later on. A value of one at a certain position would indicate that in all simulations a particle initially at that position was ejected; conversely, a value of zero means that in all simulations a particle initially at that position was not ejected. We can see in Figure 3.14 the presence of some regions with values of ejected particles in $\sim 50\%$ of the simulations (i.e. with values $\overline{\mathrm{ej}} > 0.5$).These regions with higher likelihoods of producing winds are located in the corona of the accretion disc, suggesting that the winds we are seeing correspond to thermally-driven coronal winds.

Table 3.1 - Slope in the power-law modelling for the equatorial density profile of the complete sample of performed simulations.

#ID	$\mathbf{p}^{23}$	η	Wind activity time [%]	$f_{\mathrm{ej;real}}$[%]	f_{enej}[%]	$R_*[R_S]^4$	$\overline{v}/c^5$
00	0.48	0.0005	2	4.9	1.9	303	0.0020
01	0.89	0.0022	15	2.1	0.7	235	0.0062
02	1.16	0.0021	51	8.2	2.8	239	0.0010
03	1.16	0.0018	46	4.8	1.3	162	0.0010
04	1.16	0.0022	53	7.0	2.2	298	0.0018
05	0.97	0.0079	13	0.0	0.0	–	–
06	0.91	0.1506	98	0.0	0.0	–	–
07	1.37	0.0007	95	18	19	129	0.0028
08	1.33	0.0008	97	9.0	7.8	145	0.0045
09	1.13	0.0074	45	0.0	0.0	–	–
10	1.53	0.1265	56	18.	0.9	205	0.0017

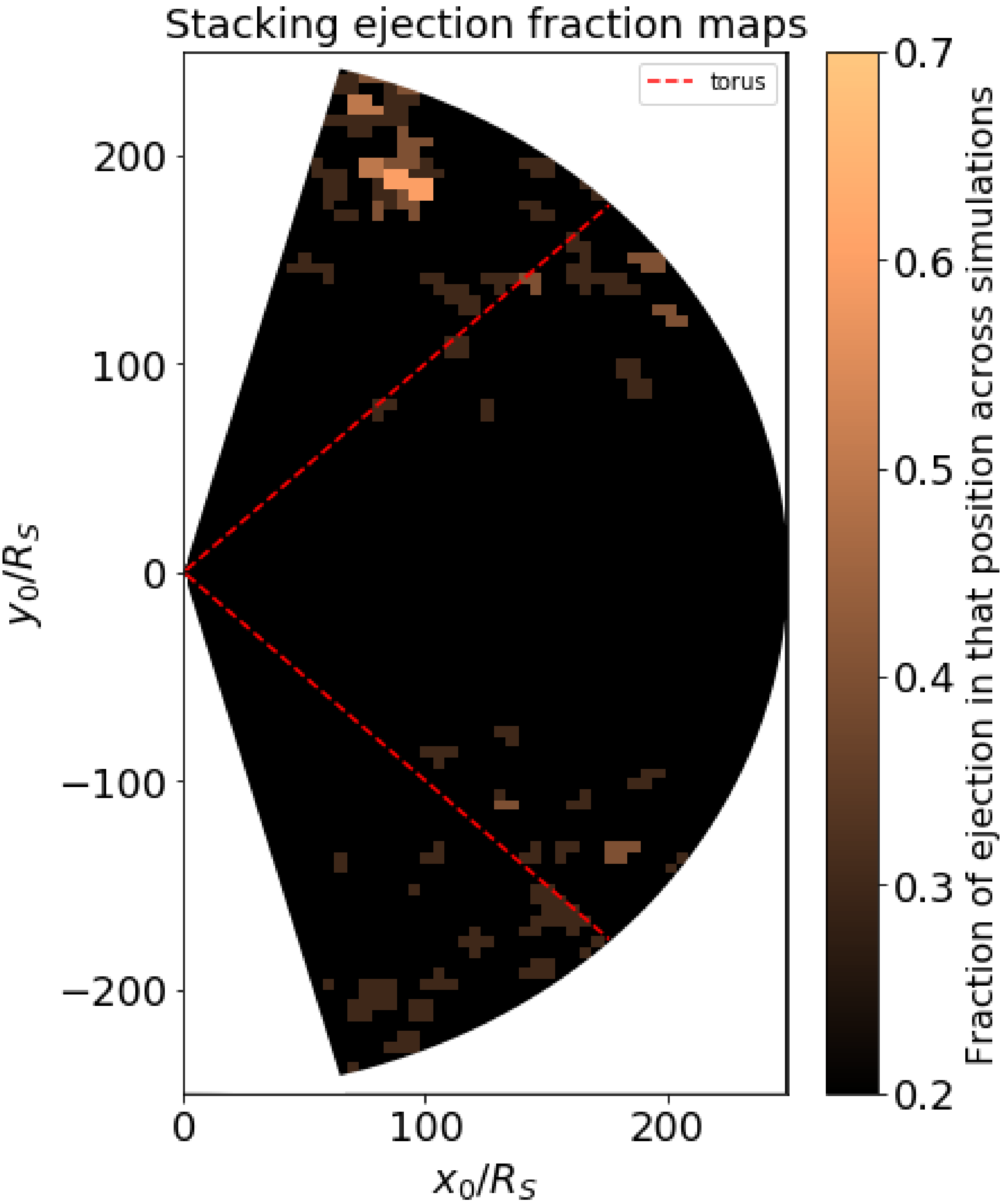

Figure 3.14: This map is a normalized stacking from all ejection maps (see figure 3.9) considering the variable ej from (3.15). The color scale means the frequency in that a particle originally located in $\mathbf{r}(t = t_0) = (x_0, y_0)$ becomes an outflowing particles in the simulations. If the value is 1 means that in all simulations a particle in $\mathbf{r}(t = t_0)$ was ejected and, oppositely, if the value is 0 means that in all simulations a particle in $\mathbf{r}(t = t_0)$ was not ejected. In this map we can see that are some regions that ejected particles in $\sim 50\%$ of the simulations, these regions are always in the corona of the accretion disc.

Chapter 4

Discussion & Conclusions

4.1 Discussion

4.1.1 Accretion flow and density radial profile

In SS-viscosity simulation, inflow and outflow had essentially the same shape in the disc region, it is not inflow-dominated as the ST-viscosity simulations. The increase in the net mass accretion rate indicates material accumulation, which is visible when we plotted the equatorial density profile $\rho(r, z = 0)$, simulations with SS-viscosity had bigger values for $\max \rho$ (in $t = 0$, $\max \rho = 1$ for all simulations). This is probably related to a feature present in #ID07 and #ID08 simulations: they had an abrupt increase in net mass accretion rate in the inner boundary after $\sim 120000GM/c^3$. These two simulations appear to accumulate material in the torus until some instant when they reach some value for density, and We did not see the same for the other simulations with SS-viscosity, there is the increase of $\max(\rho)$, but they did not reach this saturation state.

In table 3.1 we presented the power-law index p for density radial profile $\rho \propto r^{-p}$ averaged over the equatorial region of the accretion flow. From this table we can draw a number of conclusions:

1. There is no clear correlation between the initial angular momentum profile adopted and the value of p. The corollary is that we see no particular values of p associated with any of the three groups in figure 3.13.

2. For simulations with the same specific angular momentum, the SS-viscosity granted higher values of p than ST-viscosity.

3. Models #ID02-04 and #ID09 had the same value of p, besides the fact that these two

simulations are completely different. #ID02-04 had very small net mass accretion rates and small ejection, while #ID09 show high net mass accretion rate and null ejection.

The last item above is especially relevant because it demonstrates that based only on the value of p, it is not straightforward to tell whether there is a wind being produced. This result seems to contradict some previous analytical (Blandford and Begelman, 1999; Begelman, 2012) and numerical (Yuan et al., 2012) works which base their analysis on the assumption that $\rho(R)$ in the accretion disc is strongly dependent on the presence of mass-loss. These works assume that $\rho(R) \propto R^{-3/2+s}$ where s is usually in the range 0.5-1 with larger values corresponding to more profuse outflows ($s = 0$ corresponds to a no-wind ADAF; Narayan and Yi 1994). Concretely, ADIOS models suggest that $s = 1$, $p = 0.5$ corresponds to very strong winds. Our model 00 shows such a similar density profile, however it display a feeble breeze over just a short amount of time. Our model with the strongest winds–model 08–has a low value of $s = 0.17$ in contradiction with ADIOS models, and also similar to models with no winds such as 09. We conclude that we cannot make strong statements about the presence of winds based on the indirect information given by $\rho(R)$.

4.1.2 Winds and their nature

With our very long simulations, we have found that the wind production is not continuous in time as can be seen in Fig. 3.6. Some models, such as model 04, display an intermittent character alternating between ejection and "quiescent" moments. We computed the power spectrum of η and did not find any indication of periodicity in any simulation.

We have found that a small change in the value of the α-viscosity can have a notable effect on the properties of the resulting outflow. For instance, consider the models #ID07 and #ID08. A small increase in the value of α from 0.1 to 0.3 resulted in a notable increase in the amount of energy carried by the outflow in two times. Interestingly, the accretion rate did not change with this variation. A possible qualitative explanation is that for small values of α there is not enough gas reaching the wind launching region, so the wind is very weak or absent. On the other hand, with very high values of α there is enough gas being channeled in an outflow but the increased viscosity makes it lose energy and angular momentum rapidly. Therefore, there would an intermediate "sweet spot" of α-values that optimizes wind launching, such that enough gas is lost in an outflow and keeping it stable and with enough energy to reach large distances.

On average the efficiency of the winds in our models is in the range $\eta \sim 10^{-3} - 10^{-2}$, which is a bit lower than the typical values of $\eta = 0.03$ found by Sądowski et al. (2016) in their GRMHD simulations of RIAFs around nonspinning BHs. We think that the difference is due to the fact that we have not considered magnetic fields in our simulations, which can increase the intensity of outflows due to MHD processes. We intend to investigate the impact of magnetic fields on the outflows in a forthcoming work.

4.1.3 Comparison with observations

Our simulations with the ST viscosity (models 00, 01, 05 and 09), presented the value of $p \sim 0.5 - 1$. The resulting density profiles are consistent with those constrained from observations of LLAGNs, for instance Sgr A* ($p \sim 0.5$; Yuan et al. 2003; Wang et al. 2013), NGC 3115 ($p \sim 1$; Wong et al. 2011, 2014; **?**) and M87 ($p \sim 1$; Kuo et al. 2014; Russell et al. 2015). In our sample these simulations had more inefficient winds compared with the others. The simulations with SS viscosity (models 02, 03, 04, 06, 07, 08) achieved more efficient winds but with $p \sim 1.1 - 1.4$, marginally consistent with the observations of NGC 3115 and M87.

In many of our simulations, we have found that a typical value for the efficiency of wind production η (eq. 3.5) is 10^{-3}. Interestingly enough, this is in good agreement with the mechanical feedback efficiency of $10^{-4} - 10^{-3}$ required in cosmological simulations of AGN feedback in the so-called radio mode, in order to offset cooling in galaxy clusters and individual galaxies (Sijacki et al., 2007, 2015) and reproduce observations. Therefore, RIAFs could in principle provide efficient feedback to quench star formation in galaxies. Given the typical values of η found in our simulations, we can use eq. 3.5 to write

$$\dot{E}_{\rm wind} = 10^{41} \left(\frac{M}{M_\odot} \right) \left(\frac{\dot{M}}{10^{-3} \dot{M}_{\rm Edd}} \right) \text{ erg s}^{-1} \tag{4.1}$$

where $\dot{M}$ is taken as the accretion rate fed at the outer radius of the accretion flow, as defined previously (cf. section 3.1.2).

We now turn to the comparison of the energetics of our modeled winds with observations of LLAGNs. The "Akira"galaxy hosts a $10^8 M_\odot$ SMBH accreting at $\dot{M} \sim 10^{-4} \dot{M}_{Edd}$ (Cheung et al., 2016). Applying eq. 4.1 to Akira, we get $\dot{E}_{\rm wind} \sim 10^{40}$ erg s^{-1} which is consistent with the wind kinetic power derived from integral field unit observations of the ionized gas ($\approx 10^{39}$ erg s^{-1}; Cheung et al. 2016). This wind can inject sufficient energy to offset the cooling rate in both the ionized and cool gas phases in Akira. Moreover, the simple wind model of Cheung et al. gives a constant radially-outward velocity of 310 km s^{-1} in a wide-angle cone in Akira. From our simulations, the average velocity of the outflowing particles was $\sim 10^{-3}c \approx 300$ km s^{-1}, which is in excellent agreement with the observations reported by Cheung et al. (2016). In conclusion, the properties of the wind observed in the Akira galaxy–the prototypical red geyser–are well explained as winds from a RIAF as modelled in this work.

The SMBH at the center of Our Galaxy–Sgr A*–is accreting with a Bondi rate of $\dot{M}_{\rm Bondi} \approx 10^{-5} M_{\odot}/yr \approx 10^{-4} \dot{M}_{Edd}$ (Baganoff et al., 2003) which taking into account the RIAF solution gives $\dot{M} \sim 0.1 \dot{M}_{\rm Bondi} \approx 10^{-5} \dot{M}_{Edd}$. Using eq. 4.1 this gives results in a wind power of $\dot{E}_{wind} = 10^{38}$ erg s^{-1}. This estimate is similar to the power previously estimated by different authors Falcke et al. (2000); Merloni and Heinz (2007). Such winds could be important in explaining the Pevatron observations by the High Energy Stereoscopic System collaboration (HESS Collaboration et al., 2016) and the *Fermi* bubbles (Su et al., 2010).

We should note that our winds could be agents of AGN feedback in galaxies hosting SMBHs accreting in the sub-Eddington, RIAF mode. Such feedback would be neither in the radio mode–since it is not through a relativistic jet–nor in the quasar mode–since we are modeling SMBHs accreting at low rates. One class of galaxies which could be subject to this type of feedback–in fact, it seems to be required to explain them–are LLAGNs in the proposed “red geyser” mode (Cheung et al., 2016; Roy et al., 2018). In red geysers, periodic low-power outflows from the central LLAGN would be able to heat the surrounding gas, prevent any substantial star formation and thereby maintain the quiescence in typical galaxies. The outflows self-consistently modeled in this work can explain the origin of the red geyser mode of AGN feedback.

4.1.4 Comparison with previous numerical simulations

Our simulations with the ST viscosity, except #ID10, presented the value of $p \sim 0.5-1$, which agreed with the simulations performed by Stone et al. (1999); Yuan et al. (2012,?) that had used the same viscosity. The simulations with SS viscosity (models 02, 03, 04, 06, 07, 08) achieved more efficient winds but with $p \sim 1.1 - 1.4$, which is slightly below the self-similar, no-wind ADAF solution (Narayan and Yi, 1994).

On average the efficiency of the winds in our models is in the range $\eta \sim 10^{-3} - 10^{-2}$, which is a bit lower than the typical values of $\eta = 0.03$ found by Sądowski et al. (2016) in their GRMHD simulations of RIAFs around nonspinning BHs. We think that the difference is due to the fact that we have not considered magnetic fields in our simulations, which can increase the intensity of outflows due to MHD processes. We intend to investigate the impact of magnetic fields on the outflows in a forthcoming work.

4.1.5 Pathologies

These simulations are purely hydrodynamical, with the angular momentum transport role of the MRI incorporated via an effective viscous stress tensor. MHD effects such as e.g. magnetocentrifugal processes could enhance the production of outflows beyond our estimates in this work. In our simulation the material was ejected via forces created by pressure gradients in the disc–thermally-drive winds. Magnetic fields add into the material a new force component, the Lorentz force, that can enhance the production of outflows and the average energy of the ejected particles. We plan to carry out (GR)MHD simulations to investigate these effects in the future.

Our gravity is represented by the simple pseudo-Newtonian gravitational potential of Paczyńsky and Wiita (1980). This is clearly not the most accurate description of gravity. Nevertheless, it is very useful to save computer time since it avoids the extra computational costs of dealing with metric factors, with the advantage of incorporating the physics of innermost stable circular orbit. For very small radius $R \approx R_S$ our simulation is not very accurate, so we need to restrict our analysis to a slightly larger radius.

All the simulations were two-dimensional–we assumed complete axisymmetry. Three-dimensional simulations could reveal more turbulence in the disc and possible stronger anisotropies in the wind production (e.g. Narayan et al. 2012). They are much more computationally expensive, but the upgrade from 2D to 3D can improve the accuracy of the results.

4.2 Summary

The results given by the particle analysis and the accretion disc thermodynamics were consistent between themselves, they both support the scenario of winds as a generic feature of hot accretion flows, that did not depend of particular topologies of magnetic fields, once there is a mechanism that can transfer inside the fluid energy and angular momentum, that generates an effective viscosity, like MRI (Balbus, 2003). Our simulates suggested powerful thermal winds coming from hot accretion flows, these winds can carry energy away from the region of gravitational influence of the SMBH and interact with the host galaxy. The winds can heat the interstellar medium depositing energy in the gas, which can be a possible mechanism of feedback in LLAGNs without strong jets, this heating quenches the stellar formation, since stars need cold gas to born.

Presenting a brief summary of our results

- Hydrodynamical simulations with implemented viscosity can generate powerful winds, with $0.1 - 1\%$ of the accreted energy $\dot{M}c^2$.
- The unknown "initial condition"for real systems are a problem. Specific angular momentum profile $l(r)$ and the viscosity ν change drastically the accretion flow properties, even for long run simulations, the initial condition still matter. The way that the gas reaches the gravitational zone of influence of the SMBH probably affects all the accretion flow.
- Winds can be not continuous across time, the outflow generation can have times of activity interleaved with non-activity. Winds can be generate as powerful bursts too, depending of the accretion disc state.
- The slope of the equatorial density profile $\rho(r, z = 0)$ had degeneracies in our simulation sample, it was impossible to affirm something about outflows only with this value.
- The average energy per ejected particle followed an exponential relation, $\overline{E}_p \propto 10^{-\frac{R}{R_*}}$. Particles ejected from the inner regions of the disc $R < R_*$ had more available energy, and probably can reach more distant regions.

- The average velocity of our simulated particles match the measurement of the ionized gas in the "red geyser"Akira, our simulation predicts subrelativistic winds with $\sim$ 0.1% of the light speed, which is coherent with the observations of gas in Akira with speeds in the order of 300km/s (Cheung et al., 2016).

- The ejected particle, analyzing the hole sample of the simulations, come from the coronal region of the disc, $30° \lesssim \theta \lesssim 60°$, which agreed with the scenario in that the main body of the disc is dominated by inflow.

- The energy output, when compared to the galaxy Akira (Cheung et al., 2016), in our simulations predicted very higher values. Our assumption is that $\dot{m}(500R_S)$ matched the observational value, which can be not true. We can not make strong assertions about bigger regions, since we saw a increasing behaviour of $\dot{m}_{\rm inflow}(R)$, maybe we had overestimate the wind power. Besides this we did not model any interaction with the galaxy, so our results can be treated as upper limits in the wind power.

Our simulations were limited to the current computational resources, as discussed in section 4.1.5, to improve the results 3D simulations would be interesting because they allow us to see more anisotropies in the wind production and characterize better these outflows. A natural upgrade of these simulations is run magnetohydrodynamic simulations of hot accretion flows (Narayan et al., 2012; Yuan et al., 2012), which is computationally more expensive but more realistic in the sense that we expect important magnetic field effects, like the driving of angular momentum transfer. Magnetic fields could even enhance the wind power, since there will be an extra Lorentz force to eject material, which is absent in this work.

The HD case is the most simple and generic case for an accretion flow, we only take account the traditional thermodynamic features of the flow in this work and evolve it in time. We found that purely HD simulation can generate winds, so outflows of this nature should be common in any more complex setup. Our simulations suggest powerful winds with $\dot{E}_{wind} \gtrsim 10^{39}$ erg/s for systems similar to LLAGNs –with the parameterization discussed in section 4.1. We did not model the interaction with galaxy, but winds with these power can interact with the gas in the and heat the environment, acting as one possible mechanism of feedback.

Bibliography

Hyperbolic partial differential equation, Encyclopedia of Mathematics `http://www.encyclopediaofmath.org/index.php?title=Hyperbolic_partial_differential_equation&oldid=28218`, note = Accessed: 2019-01-17, 2019

Abbott B. P., Abbott R., Abbott T. D., Abernathy M. R., Acernese F., Ackley K., Adams C., Adams T., Addesso P., Adhikari R. X., et al. Astrophysical Implications of the Binary Black Hole Merger GW150914, ApJ, 2016, vol. 818, p. L22

Abramowicz M. A., Fragile P. C., Foundations of Black Hole Accretion Disk Theory, Living Reviews in Relativity, 2013, vol. 16, p. 1

Abuter R., Amorim A., Bauböck M., Berger J., Bonnet H., Brandner W., Clénet Y., du Foresto V. C., de Zeeuw P., Deen C., et al., Detection of orbital motions near the last stable circular orbit of the massive black hole SgrA, Astronomy & Astrophysics, 2018, vol. 618, p. L10

Ackermann M., Albert A., Atwood W., Baldini L., Ballet J., Barbiellini G., Bastieri D., Bellazzini R., Bissaldi E., Blandford R., et al., The spectrum and morphology of the Fermi bubbles, The Astrophysical Journal, 2014, vol. 793, p. 64

Almeida I., Nemmen R., Wong K.-W., Wu Q., Irwin J. A., The multiwavelength spectrum of NGC 3115: Hot accretion flow properties, Monthly Notices of the Royal Astronomical Society, 2018, vol. 475, p. 5398

Baganoff F. K., Maeda Y., Morris M., Bautz M. W., Brandt W. N., Cui W., Doty J. P., Feigelson E. D., Garmire G. P., Pravdo S. H., Ricker G. R., Townsley L. K., Chandra

X-Ray Spectroscopic Imaging of Sagittarius A* and the Central Parsec of the Galaxy, ApJ, 2003, vol. 591, p. 891

Balbus S. A., Enhanced Angular Momentum Transport in Accretion Disks, ARA&A, 2003, vol. 41, p. 555

Balbus S. A., Hawley J. F., Instability, turbulence, and enhanced transport in accretion disks, Reviews of Modern Physics, 1998, vol. 70, p. 1

Beckmann V., Shrader C. R., Active Galactic Nuclei. Wiley, 2012

Begelman M. C., Radiatively inefficient accretion: breezes, winds and hyperaccretion, MNRAS, 2012, vol. 420, p. 2912

Bell E. F., Wolf C., Meisenheimer K., Rix H.-W., Borch A., Dye S., Kleinheinrich M., Wisotzki L., McIntosh D. H., Nearly 5000 Distant Early-Type Galaxies in COMBO-17: A Red Sequence and Its Evolution since$z \sim 1$, ApJ, 2004, vol. 608, p. 752

Bîrzan L., Rafferty D. A., McNamara B. R., Wise M. W., Nulsen P. E. J., A Systematic Study of Radio-induced X-Ray Cavities in Clusters, Groups, and Galaxies, ApJ, 2004, vol. 607, p. 800

Blandford R. D., Begelman M. C., On the fate of gas accreting at a low rate on to a black hole, MNRAS, 1999, vol. 303, p. L1

Blandford R. D., Znajek R. L., Electromagnetic extraction of energy from Kerr black holes, MNRAS, 1977, vol. 179, p. 433

Bower R. G., Benson A. J., Malbon R., Helly J. C., Frenk C. S., Baugh C. M., Cole S., Lacey C. G., Breaking the hierarchy of galaxy formation, MNRAS, 2006, vol. 370, p. 645

Bower R. G., Schaye J., Frenk C. S., Theuns T., Schaller M., Crain R. A., McAlpine S., The dark nemesis of galaxy formation: why hot haloes trigger black hole growth and bring star formation to an end, MNRAS, 2017, vol. 465, p. 32

Bu D.-F., Yuan F., Gan Z.-M., Yang X.-H., Magnetohydrodynamic Numerical Simulation of Wind Production from Hot Accretion Flows around Black Holes at Very Large Radii, ApJ, 2016, vol. 823, p. 90

Bundy K., Ellis R. S., Conselice C. J., Taylor J. E., Cooper M. C., Willmer C. N. A., Weiner B. J., Coil A. L., Noeske K. G., Eisenhardt P. R. M., The Mass Assembly History of Field Galaxies: Detection of an Evolving Mass Limit for Star-Forming Galaxies, ApJ, 2006, vol. 651, p. 120

Chan C.-K., Psaltis D., Özel F., Narayan R., Sa̧dowski A., The Power of Imaging: Constraining the Plasma Properties of GRMHD Simulations using EHT Observations of Sgr A*, ApJ, 2015, vol. 799, p. 1

Cheung E., Bundy K., Cappellari M., Peirani S., Rujopakarn W., Westfall K., Yan R., Bershady M., Greene J. E., Heckman T. M., et al., Suppressing star formation in quiescent galaxies with supermassive black hole winds, Nature, 2016, vol. 533, p. 504

Courant R., Friedrichs K., Lewy H., Über die partiellen Differenzengleichungen der mathematischen Physik, Mathematische annalen, 1928, vol. 100, p. 32

Croton D. J., Springel V., White S. D. M., De Lucia G., Frenk C. S., Gao L., Jenkins A., Kauffmann G., Navarro J. F., Yoshida N., The many lives of active galactic nuclei: cooling flows, black holes and the luminosities and colours of galaxies, MNRAS, 2006, vol. 365, p. 11

Di Matteo T., Springel V., Hernquist L., Energy input from quasars regulates the growth and activity of black holes and their host galaxies, Nature, 2005, vol. 433, p. 604

Doeleman S. S., Weintroub J., Rogers A. E., Plambeck R., Freund R., Tilanus R. P., Friberg P., Ziurys L. M., Moran J. M., Corey B., et al., Event-horizon-scale structure in the supermassive black hole candidate at the Galactic Centre, Nature, 2008, vol. 455, p. 78

Dubois Y., Pichon C., Haehnelt M., Kimm T., Slyz A., Devriendt J., Pogosyan D., Feeding compact bulges and supermassive black holes with low angular momentum cosmic gas at high redshift, MNRAS, 2012, vol. 423, p. 3616

Enßlin T. A., Brüggen M., On the formation of cluster radio relics, MNRAS, 2002, vol. 331, p. 1011

Faber S., Willmer C., Wolf C., Koo D., Weiner B., Newman J. A., Im M., Coil A., Conroy C., Cooper M., et al., Galaxy luminosity functions to z˜ 1 from DEEP2 and COMBO-17: implications for red galaxy formation, The Astrophysical Journal, 2007, vol. 665, p. 265

Falcke H., Melia F., Agol E., Viewing the Shadow of the Black Hole at the Galactic Center, ApJ, 2000, vol. 528, p. L13

Ferrarese L., Ford H., Supermassive Black Holes in Galactic Nuclei: Past, Present and Future Research, Space Sci. Rev., 2005, vol. 116, p. 523

Frank J., King A., Raine D. J., Accretion Power in Astrophysics 3rd edn. Cambridge University Press, 2002

Genel S., Vogelsberger M., Nelson D., Sijacki D., Springel V., Hernquist L., Following the flow: tracer particles in astrophysical fluid simulations, MNRAS, 2013, vol. 435, p. 1426

Guo F., Mathews W. G., The Fermi Bubbles. I. Possible Evidence for Recent AGN Jet Activity in the Galaxy, ApJ, 2012, vol. 756, p. 181

Harlow F. H., Welch J. E., Numerical Calculation of Time-Dependent Viscous Incompressible Flow of Fluid with Free Surface, Physics of Fluids, 1965, vol. 8, p. 2182

Heinz S., Merloni A., Schwab J., The Kinetic Luminosity Function and the Jet Production Efficiency of Growing Black Holes, ApJ, 2007, vol. 658, p. L9

HESS Collaboration Abramowski A., Aharonian F., Benkhali F. A., Akhperjanian A. G., Angüner E. O., Backes M., Balzer A., Becherini Y., Tjus J. B., et al. Acceleration of petaelectronvolt protons in the Galactic Centre, Nature, 2016, vol. 531, p. 476

Ho L. C., On the Relationship between Radio Emission and Black Hole Mass in Galactic Nuclei, ApJ, 2002, vol. 564, p. 120

Ho L. C., Nuclear Activity in Nearby Galaxies, ARA&A, 2008, vol. 46, p. 475

Ichimaru S., Bimodal behavior of accretion disks-Theory and application to Cygnus X-1 transitions, The Astrophysical Journal, 1977, vol. 214, p. 840

Ilbert O., Salvato M., Le Floc'h E., Aussel H., Capak P., McCracken H., Mobasher B., Kartaltepe J., Scoville N., Sanders D., et al., Galaxy stellar mass assembly between 0.2¡ z¡ 2 from the S-COSMOS survey, The Astrophysical Journal, 2010, vol. 709, p. 644

Kellermann K. I., Sramek R., Schmidt M., Shaffer D. B., Green R., VLA observations of objects in the Palomar Bright Quasar Survey, AJ, 1989, vol. 98, p. 1195

Kuo C. Y., Asada K., Rao R., Nakamura M., Algaba J. C., Liu H. B., Inoue M., Koch P. M., Ho P. T. P., Matsushita S., Pu H.-Y., Akiyama K., Nishioka H., Pradel N., Measuring Mass Accretion Rate onto the Supermassive Black Hole in M87 Using Faraday Rotation Measure with the Submillimeter Array, ApJ, 2014, vol. 783, p. L33

Landau L. D., Lifshitz E. M., Fluid mechanics, 1959

McNamara B. R., Nulsen P. E. J., Mechanical feedback from active galactic nuclei in galaxies, groups and clusters, New Journal of Physics, 2012, vol. 14, p. 055023

Meier D. L., Black Hole Astrophysics: The Engine Paradigm. Springer, Verlag Berlin Heidelberg, 2012

Merloni A., Heinz S., Measuring the kinetic power of active galactic nuclei in the radio mode, MNRAS, 2007, vol. 381, p. 589

Merloni A., Heinz S., A synthesis model for AGN evolution: supermassive black holes growth and feedback modes, MNRAS, 2008, vol. 388, p. 1011

Mignone A., Bodo G., Massaglia S., Matsakos T., Tesileanu O., Zanni C., Ferrari A., PLUTO: A Numerical Code for Computational Astrophysics, ApJS, 2007, vol. 170, p. 228

Mościbrodzka M., Falcke H., Coupled jet-disk model for Sagittarius A*: explaining the flat-spectrum radio core with GRMHD simulations of jets, A&A, 2013, vol. 559, p. L3

Nagar N. M., Falcke H., Wilson A. S., Ho L. C., Radio Sources in Low-Luminosity Active Galactic Nuclei. I. VLA Detections of Compact, Flat-Spectrum Cores, ApJ, 2000, vol. 542, p. 186

Nagar N. M., Wilson A. S., Falcke H., Evidence for Jet Domination of the Nuclear Radio Emission in Low-Luminosity Active Galactic Nuclei, ApJ, 2001, vol. 559, p. L87

Narayan R., Sadowski A., Penna R. F., Kulkarni A. K., GRMHD simulations of magnetized advection-dominated accretion on a non-spinning black hole: role of outflows, MNRAS, 2012, vol. 426, p. 3241

Narayan R., Yi I., Advection-dominated accretion: A self-similar solution, ApJ, 1994, vol. 428, p. L13

Narayan R., Yi I., Mahadevan R., Explaining the spectrum of Sagittarius A* with a model of an accreting black hole, Nature, 1995, vol. 374, p. 623

Nemmen R. S., Bower R. G., Babul A., Storchi-Bergmann T., Models for jet power in elliptical galaxies: a case for rapidly spinning black holes, MNRAS, 2007, vol. 377, p. 1652

Nemmen R. S., Storchi-Bergmann T., Eracleous M., Spectral models for low-luminosity active galactic nuclei in LINERs: the role of advection-dominated accretion and jets, MNRAS, 2014, vol. 438, p. 2804

Netzer H., Revisiting the Unified Model of Active Galactic Nuclei, ARA&A, 2015, vol. 53, p. 365

Newman E. T., Couch E., Chinnapared K., Exton A., Prakash A., Torrence R., Metric of a rotating, charged mass, Journal of mathematical physics, 1965, vol. 6, p. 918

Paczyńsky B., Wiita P. J., Thick accretion disks and supercritical luminosities, A&A, 1980, vol. 88, p. 23

Papaloizou J. C. B., Pringle J. E., The dynamical stability of differentially rotating discs with constant specific angular momentum, MNRAS, 1984, vol. 208, p. 721

Penna R. F., Kulkarni A., Narayan R., A new equilibrium torus solution and GRMHD initial conditions, A&A, 2013, vol. 559, p. A116

Penna R. F., Sądowski A., Kulkarni A. K., Narayan R., The Shakura-Sunyaev viscosity prescription with variable α (r), MNRAS, 2013, vol. 428, p. 2255

Ponti G., Terrier R., Goldwurm A., Belanger G., Trap G., Discovery of a Superluminal Fe K Echo at the Galactic Center: The Glorious Past of Sgr A* Preserved by Molecular Clouds, ApJ, 2010, vol. 714, p. 732

Porth O., Olivares H., Mizuno Y., Younsi Z., Rezzolla L., Moscibrodzka M., Falcke H., Kramer M., The black hole accretion code, Computational Astrophysics and Cosmology, 2017, vol. 4, p. 1

Roy N., Bundy K., Cheung E., Rujopakarn W., Cappellari M., Belfiore F., Yan R., Heckman T., Bershady M., Greene J., et al., Detecting Radio AGN Signatures in Red Geysers, The Astrophysical Journal, 2018, vol. 869, p. 117

Russell H. R., Fabian A. C., McNamara B. R., Broderick A. E., Inside the Bondi radius of M87, MNRAS, 2015, vol. 451, p. 588

Sądowski A., Lasota J.-P., Abramowicz M. A., Narayan R., Energy flows in thick accretion discs and their consequences for black hole feedback, MNRAS, 2016, vol. 456, p. 3915

Sądowski A., Narayan R., Penna R., Zhu Y., Energy, momentum and mass outflows and feedback from thick accretion discs around rotating black holes, MNRAS, 2013, vol. 436, p. 3856

Schmidt M., 3C273: a star-like object with large red-shift.Â, 1963

Schneider P., , 2006 Extragalactic Astronomy and Cosmology, by Peter Schneider

Shakura N. I., Sunyaev R. A., Black holes in binary systems. Observational appearance., A&A, 1973, vol. 24, p. 337

Sijacki D., Springel V., Di Matteo T., Hernquist L., A unified model for AGN feedback in cosmological simulations of structure formation, MNRAS, 2007, vol. 380, p. 877

Sijacki D., Vogelsberger M., Genel S., Springel V., Torrey P., Snyder G. F., Nelson D., Hernquist L., The Illustris simulation: the evolving population of black holes across cosmic time, MNRAS, 2015, vol. 452, p. 575

Stone J. M., Pringle J. E., Begelman M. C., Hydrodynamical non-radiative accretion flows in two dimensions, MNRAS, 1999, vol. 310, p. 1002

Sturm E., Dexter J., Pfuhl O., Stock M., Davies R., Lutz D., Clénet Y., Eckart A., Eisenhauer F., Genzel R., et al., Spatially resolved rotation of the broad-line region of a quasar at sub-parsec scale, arXiv preprint arXiv:1811.11195, 2018

Su M., Slatyer T. R., Finkbeiner D. P., Giant Gamma-ray Bubbles from Fermi-LAT: Active Galactic Nucleus Activity or Bipolar Galactic Wind?, ApJ, 2010, vol. 724, p. 1044

Tchekhovskoy A., Narayan R., McKinney J. C., Efficient generation of jets from magnetically arrested accretion on a rapidly spinning black hole, MNRAS, 2011, vol. 418, p. L79

Thorne K., Price R., Cygnus X-1-an interpretation of the spectrum and its variability, The Astrophysical Journal, 1975, vol. 195, p. L101

Toro E. F., Riemann solvers and numerical methods for fluid dynamics: a practical introduction. Springer Science & Business Media, 2013

van Leer B., Godunov's Method for Gas-Dynamics: Current Applications and Future Developments, Journal of Computational Physics, 1997, vol. 132, p. 1

Wang Q. D., Nowak M. A., Markoff S. B., Baganoff F. K., Nayakshin S., Yuan F., Cuadra J., Davis J., Dexter J., Fabian A. C., Grosso N., Haggard D., Houck J., Ji L., Li Z., Neilsen J., Porquet D., Ripple F., Shcherbakov R. V., Dissecting X-ray–Emitting Gas Around the Center of Our Galaxy, Science, 2013, vol. 341, p. 981

Wong K.-W., Irwin J. A., Shcherbakov R. V., Yukita M., Million E. T., Bregman J. N., The Megasecond Chandra X-Ray Visionary Project Observation of NGC3115: Witnessing the Flow of Hot Gas within the Bondi Radius, ApJ, 2014, vol. 780, p. 9

Wong K.-W., Irwin J. A., Yukita M., Million E. T., Mathews W. G., Bregman J. N., Resolving the Bondi Accretion Flow toward the Supermassive Black Hole of NGC 3115 with Chandra, ApJ, 2011, vol. 736, p. L23

Younes G., Porquet D., Sabra B., Reeves J. N., Grosso N., Study of LINER sources with broad Hα emission. Spectral energy distribution and multiwavelength correlations, A&A, 2012, vol. 539, p. A104

Yuan F., Bu D., Wu M., Numerical Simulation of Hot Accretion Flows. II. Nature, Origin, and Properties of Outflows and their Possible Observational Applications, ApJ, 2012, vol. 761, p. 130

Yuan F., Gan Z., Narayan R., Sadowski A., Bu D., Bai X.-N., Numerical Simulation of Hot Accretion Flows. III. Revisiting Wind Properties Using the Trajectory Approach, ApJ, 2015, vol. 804, p. 101

Yuan F., Narayan R., Hot Accretion Flows Around Black Holes, ARA&A, 2014, vol. 52, p. 529

Yuan F., Quataert E., Narayan R., Nonthermal Electrons in Radiatively Inefficient Accretion Flow Models of Sagittarius A*, ApJ, 2003, vol. 598, p. 301

Yuan F., Wu M., Bu D., Numerical Simulation of Hot Accretion Flows. I. A Large Radial Dynamical Range and the Density Profile of Accretion Flow, ApJ, 2012, vol. 761, p. 129